Determining the jet energy resolution in proton-proton collisions at $\sqrt{s} = 13$ TeV recorded in 2017 with the ATLAS detector using the bisector method

Ellinor Eckstein

I hereby declare that this thesis was formulated by myself and that no sources or tools other than those cited were used.

Bonn, ...
            Date   Signature

1. Gutachter: Prof. Dr. Ian C. Brock
2. Gutachter: Prof. Dr. Klaus Desch

Contents

Introduction

1.1 Motivation

Mankind has always been driven to get an understanding of its surroundings, for example, the question "Why does the apple fall to the ground?" has allegedly inspired Isaac Newton to develop his law of gravitation. Over the past decades and centuries, there has been major progress in physics and science in general. Only in the late 19th century electricity became accessible for the common population of industrial countries, in 1941 the first electromechanical programmable computer was engineered by Konrad Zuse and in 1989 the world wide web was invented by Tim Burners Lee devoid of which our world today would not look the same.

All those inventions went along with new insights regarding basically every research field where mankind takes an interest in. Throughout the years, scientists became to understand the laws of nature to ever greater detail. Based on the knowledge gained so far, the standard model of particle physics has been enunciated which describes all known fundamental particles as of today and their interaction among each other. But even this widely acknowledged theory is still incomplete. Gravity, for example, remains unexplained on small scales.

On larger scales, the questions of inflation, the matter antimatter asymmetry in the early universe and the nature of dark matter and dark energy are still open, and scientists at high energy collider experiments like ATLAS are seeking for answers. Those collisions provide insight into the substructure of particles as they fragment into their constituents. Furthermore, at sufficiently high center of mass energies, new particles can be created due to the mass-energy equivalence formulated in Albert Einsteins famous equation $E = mc^2$ where E and m correspond to the energy and mass of the particle, respectively, and c equals the speed of light.

In order to probe the physics beyond the standard model, or to find new particles which would solve some of the named problems, the collisions have to be observed with high precision demanding a high resolution of the detector.

Often particles do not occur alone in high energy collider experiments but produce a collection of secondary particles which combined are called a jet. In this thesis, the jet energy resolution of the ATLAS detector will be determined using the bisector method with a modified fitting procedure, compared to previous approaches, to achieve more precise results.

1.2 Thesis overview

To do so, the necessary theoretical background knowledge (namely the standard model of particle physics) is given and jets are introduced in Chapter 2. Hereafter, a closer look into the ATLAS detector and its individual components is taken in Chapter 3, followed by more detailed information about jets and how they are reconstructed from the detector output in Chapter 4. Two different methods to determine the jet energy resolution, the direct balance and bisector method, are presented in Chapter 5 with particular emphasis on the implementation of the bisector method and the changes made to the fitting procedure in Chapter 6. Finally, the results are presented and discussed in the Chapters 7 and 8.

Theory

For a good understanding of this thesis, the necessary basic knowledge of particle physics is presented in this chapter. It will first give a short introduction to the standard model of particle physics and will then continue to have a brief look into jets as they are the objects of interest in this thesis. All information provided in this chapter without an explicit reference is taken from reference [1].

2.1 The standard model of particle physics

The standard model of particle physics describes the fundamental particles and their properties as well as the fundamental forces except gravity which remains unexplained on small scales.

2.1.1 Particles

The fundamental particles can be divided by their spin into two categories, the fermions and bosons which can also be referred to as matter particles and exchange particles, respectively. All known particles and their main properties namely mass, spin and charge are displayed in Figure 2.1.

Fermions

Fermions, the matter particles, are particles with a half integer spin, they make up all the matter surrounding us. There are two basic types of fermions, the leptons and quarks. Each type contains six distinguishable particles which can be assigned into three groups (generations) with increasing masses from first to third generation. The matter around us consists mostly of particles of the first and therefore lightest generation due to the fact that they are the most stable and heavier particles eventually decay into those first generation particles.

The lepton generations consist of one particle with an electric charge of -1e (the electron e^-, the muon μ^- or the tau τ^-) and its associated neutrino (ν_e, ν_μ, ν_τ) with a considerably smaller mass and no electric charge.

The three generations of quarks as well consist of two particles each, they are called up and down quark, charm and strange quark and top and bottom quark. These pairs of quarks are associated with a charge of $\frac{2}{3}e$ and $-\frac{1}{3}e$, respectively. In addition to their electric charge, quarks are color charged, either red, green or blue which describes their ability to interact via the strong force.

Along with those particles introduced there is another set of fundamental particles with the same structure and properties but opposite charges, denoted as antiparticles. This does not only regard the

electric charge with an inverse charge of the opposite sign, but also the color charge which is inverted to the anticolors antired, antiblue and antigreen.

Bosons

Bosons are those particles with an integral spin like gluons, photons, Z and $W^\pm$ bosons with a spin of 1 and the Higgs boson with a spin of 0.

The gluon mediates the strong interaction, it does not have a mass nor an electric charge but is the only boson which is color charged.

The photon is the exchange particle of the electromagnetic interaction, it has no mass, electric or color charge.

The Z and $W^\pm$ bosons mediate the weak interaction, the Z boson is electrically neutral whereas the $W^\pm$ boson has a charge of $\pm 1e$. Contrary to the photons and gluons, they are massive particles, the exact properties can be seen in Figure 2.1.

The Higgs boson is a unique particle in the standard model. It was predicted first by Peter Higgs in 1964 and confirmed by the ATLAS and CMS collaboration in 2012 [2, 3]. Simplified, the Higgs boson is a consequence of the phenomenon that fundamental particles have a mass as they gain it by interaction with the Higgs field.

2.1.2 Forces

There are four fundamental forces: gravitation, the weak force, the electromagnetic force and the strong force, ordered from weakest to strongest interaction on small scales. The coupling strength of the weak and strong force is heavily dependent on the distance scale. Unlike the gravitational and electromagnetic force, they both have a finite range, hence, they only dominate at a subatomic level.

For the weak interaction, this is due to the heavy gauge bosons because their large masses correspond to a short lifetime.

The associated gauge bosons with the strong interaction, the gluons, are massless. In contrast to the photons, however, they have a color charge which enables them to interact not just with the quarks but also among each other. In consequence, the attracting force between two color charged objects does not decrease when they get separated but is approximately constant for small scales and then increases rapidly at larger scales. Eventually, it is energetically more favorable for the gluon field between those particles to create a second pair of quark and antiquark forming two color neutral states. This particularity of the strong interaction which prevents color charged objects to exist isolated is called confinement.

There are two basic possibilities to build a color neutral particle, either you have three quarks of different color (or three antiquarks with three different anticolors), or you have a quark antiquark pair with corresponding color and anticolor, respectively. Since quarks, as color charged particles, must not exist isolated, they form such color neutral subatomic particles called hadrons. Those which consist of three quarks or antiquarks like protons and neutrons are called baryons, quark antiquark pairs are called mesons. However, those are not the only bound multiquark states to exist, more complex particles like tetraquarks, consisting of two quarks and two antiquarks, and pentaquarks, consisting of four quarks and one antiquark, have been predicted since the 1960s and were confirmed in recent years, amongst others by LHCb at CERN [4–6].

Standard Model of Elementary Particles

	three generations of matter (fermions)			interactions / force carriers (bosons)	
	I	II	III		

	mass $\simeq$2.2 MeV/c² charge ⅔ spin ½ **u** up	$\simeq$1.28 GeV/c² ⅔ ½ **c** charm	$\simeq$173.1 GeV/c² ⅔ ½ **t** top	0 0 1 **g** gluon	$\simeq$124.97 GeV/c² 0 0 **H** higgs
	$\simeq$4.7 MeV/c² −⅓ ½ **d** down	$\simeq$96 MeV/c² −⅓ ½ **s** strange	$\simeq$4.18 GeV/c² −⅓ ½ **b** bottom	0 0 1 **γ** photon	
	$\simeq$0.511 MeV/c² −1 ½ **e** electron	$\simeq$105.66 MeV/c² −1 ½ **μ** muon	$\simeq$1.7768 GeV/c² −1 ½ **τ** tau	$\simeq$91.19 GeV/c² 0 1 **Z** Z boson	
	<1.0 eV/c² 0 ½ **νe** electron neutrino	<0.17 MeV/c² 0 ½ **νμ** muon neutrino	<18.2 MeV/c² 0 ½ **ντ** tau neutrino	$\simeq$80.39 GeV/c² ±1 1 **W** W boson	

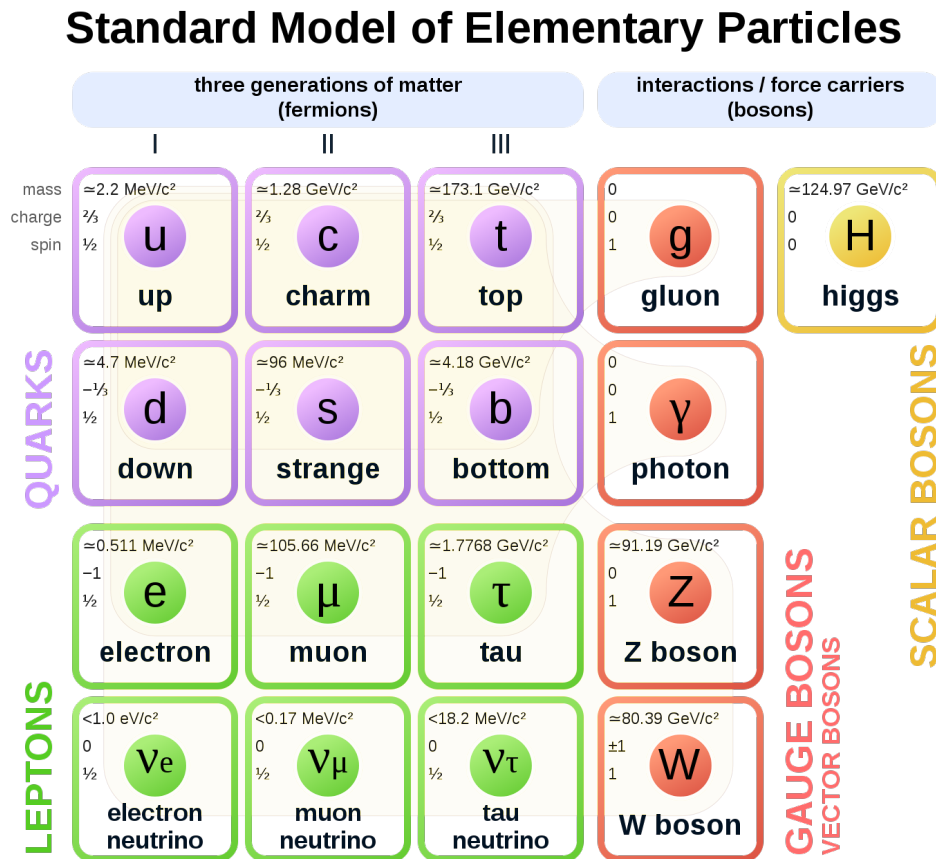QUARKS · LEPTONS · GAUGE BOSONS (VECTOR BOSONS) · SCALAR BOSONS

Figure 2.1: The standard model of particle physics can be seen here. The first three columns depict the three generations of fermions with the quarks (purple) in the top two rows and the leptons (green) in the bottom two rows, the fourth and fifth column show the bosons with the gauge bosons in red and the Higgs boson in yellow [7].

2.2 Jets

As stated above, the confinement only allows color neutral states to exist. At high energy experiments, it occurs that a color neutral object fragments in its color charged constituents. In this case, the strong gluon field creates new color charged particles to form neutral states again. At sufficiently high energies, this proceeds multiple times resulting in numerous hadronic objects which tend to follow the direction of the first particle causing their origin. The collection of those particles is called a jet.

Experimental setup

The ATLAS experiment is one of the four main experiments at the Large Hadron Collider (LHC) a particle accelerator at CERN based in Geneva.

3.1 The LHC complex

The ATLAS detector is constructed to investigate proton-proton collisions at high energies. For this purpose, two proton beams in opposite directions are injected into the LHC ring. To achieve center of mass energies up to $\sqrt{s} = 13$ TeV there are several preaccelarators involved which are displayed in Figure 3.1. The two types of particle accelerators at CERN are linear accelerators, such as LINAC2, and synchrotrons e.g. the super proton synchrotron (SPS).

In linear accelerators, particles gain energy by traversing multiple oscillating electromagnetic fields along a straight beamline. A synchrotron, on the other hand, is structured into alternating acceleration and bending segments. It uses magnetic fields to bend the particles onto a circular trajectory which allows them to pass the acceleration segments numerous times. The strength of the magnetic fields has to be precisely synchronized to the particles increasing kinetic energy for them to remain on their trajectory, hence the name synchrotron. Since the principle of acceleration for both types of accelerators is based on interaction with electromagnetic fields, they are exclusively operated with charged particles. With a circumference of approximately 27 km, located 100 m below ground level, the LHC is the worlds largest synchrotron.

It is equipped with four collision points where the main experiments are installed. These are ALICE where the state of the universe shortly after the big bang is studied, ATLAS and CMS, two general purpose detectors where the standard model of particle physics can be tested and new insights to physics beyond the standard model can be gained and LHCb which is another general purpose detector but mainly designed to measure the decay of B mesons[1] to investigate the matter antimatter asymmetry in the early universe.

3.2 The ATLAS detector

The ATLAS detector, illustrated in Figure 3.2, is composed of multiple detectors for different purposes. In total, the detector is 44 m long with 22 m in diameter and weighs 7 000 t [9]. It consists of an inner detector, calorimeters, a muon spectrometer and a magnet system which are layered concentrically around

---

[1] Mesons containing a bottom quark or antiquark in combination with a first generation antiquark and quark, respectively.
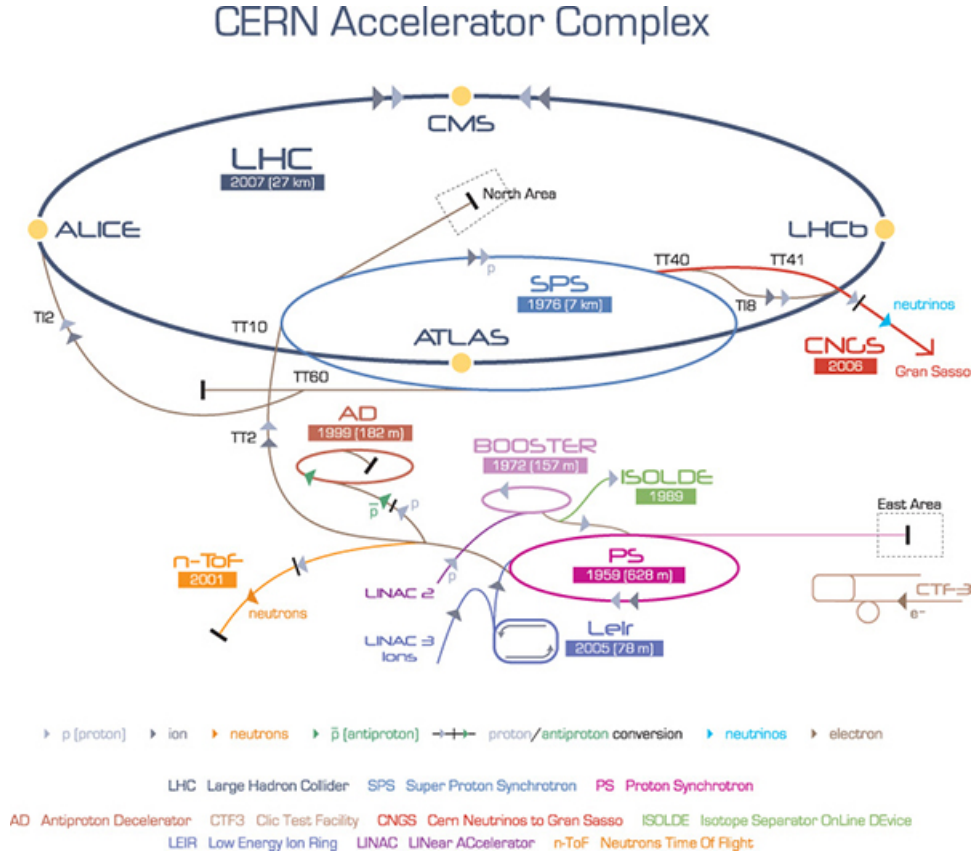
Figure 3.1: Before entering the LHC ring, the protons successively pass several preaccelerators which are sketched. From the very beginning in a hydrogen bottle, they traverse the LINAC2 (a linear accelerator, hence the name) and three proton synchrotrons (BOOSTER, PS, SPS) where the protons are accelerated up to energies of 0.45 TeV. Through the transfer line TI 8 the beam is injected into the LHC ring where the final acceleration to $\sqrt{s} = 6.5$ TeV proceeds. The positions of the four main experiments ALICE, CMS, LHCb and ATLAS are highlighted as yellow dots [8].

the beam pipe. The ATLAS coordinate system is shown in Figure 3.3, the z-axis is chosen in direction of the beamline, the angle ϕ lies in the plane perpendicular to it and θ in the y-z-plane starting from the z-axis. A more commonly used spatial coordinate is the pseudorapidity

$$\eta \equiv \frac{1}{2} \ln \left(\frac{|p| + p_z}{|p| - p_z} \right) = -\ln \left[\tan \left(\frac{\theta}{2} \right) \right] \tag{3.1}$$

where p equals the particles three-momentum and p_z its component in direction of the z-axis. It resembles the rapidity

$$y \equiv \frac{1}{2} \ln \left(\frac{E + p_z}{E - p_z} \right) \tag{3.2}$$

in the limit of particles traveling with velocities close to the speed of light where $E \approx |p|$. The distance between two objects in the η-ϕ-plane is defined as

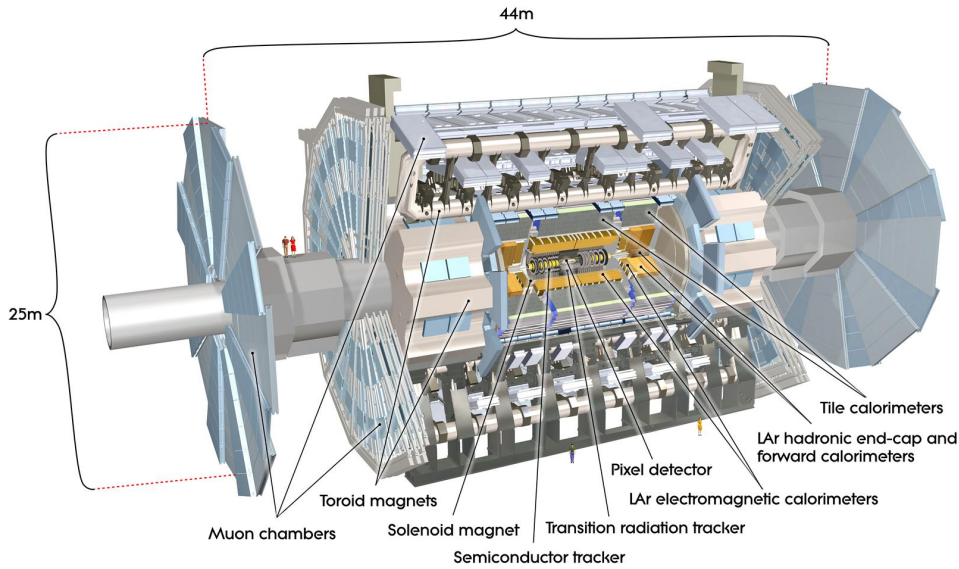$$\Delta R \equiv \sqrt{(\Delta \eta)^2 + (\Delta \phi)^2}. \tag{3.3}$$

8

Figure 3.2: A computer generated image of the ATLAS detector composed of the inner detector, the electromagnetic calorimeter as second layer, the hadronic calorimeter and the muon spectrometer [10].
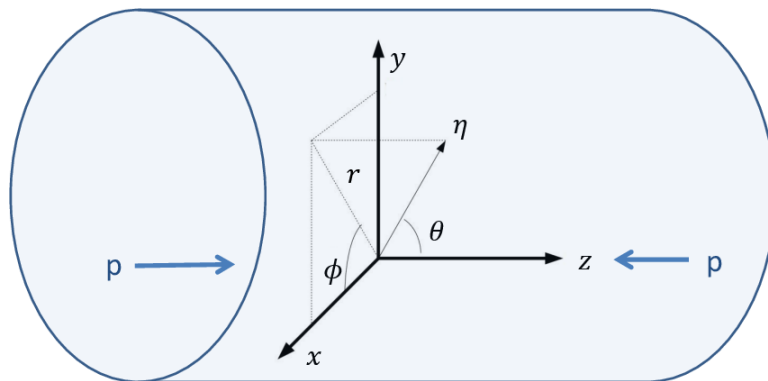

Figure 3.3: The ATLAS coordinatesystem with the z-axis along the beamline, the angle ϕ in the plane perpendicular to the beamline and θ in the y-z-plane starting from the z-axis [11].

3.2.1 The inner detector

The three main components of the inner detector, illustrated in Figure 3.4, are the pixel detector, the semiconductor tracker and the transition radiation tracker enclosed by a superconducting solenoid which creates a magnetic field parallel to the z-axis.

The pixel detector is divided into smaller units (modules) which consist of 46 080 pixels each. Arranged in three barrel layers concentrically along the beamline and three disks at each end, the modules cover an area of $1.7 \, \mathrm{m}^2$ [12]. The semiconductor tracker consists of 4088 modules of silicon strip detectors layered in four concentric barrels and nine disks at each end [13].

Both detectors record particles based on the electron hole pairs they create when entering a semiconducting material. Due to the precise separation into modules, accurate information about the trajectory of

a particle can be gained. Those particles do not traverse the detectors in a straight line but are deflected by the magnetic field provided by the superconducting solenoid. The radius and direction of the curvature of a particles' trajectory contains information about its momentum and charge, respectively, which can be extracted from the data.

The transition radiation tracker consists of 370 000 straw tubes, each 4 mm in diameter. The tube is filled with a gas mixture of xenon (70%), carbondioxide (27%) and oxygen (3%) and contains a thin wire in its center. Between tube wall and wire a high voltage is applied. Particles traversing the tracker ionize the gas thus electron ion pairs are created which then drift apart towards the wire and tube wall, respectively. Due to the high voltage, they get accelerated as they cross the gas filled tube and produce more electron ion pairs amplifying the read out signal. Assessment of the energy deposition distribution even allows to identify particles such as electrons and pions [14].
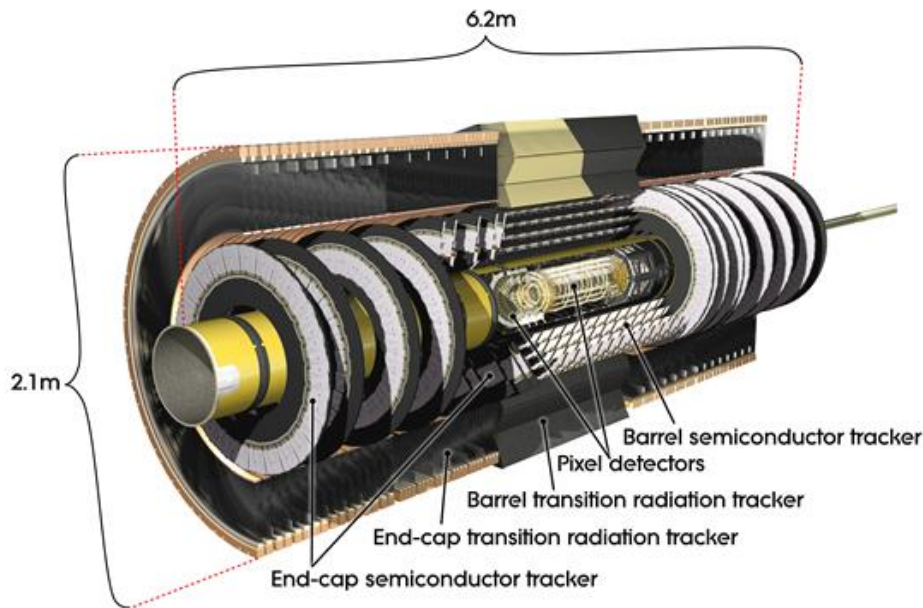

Figure 3.4: The cross-section of the inner detector is illustrated. The center part shows the pixel detectors enclosed by the barrel semiconductor tracker and the transition radiation tracker [15].

3.2.2 The calorimeters

The ATLAS detector contains two calorimeters, the electromagnetic and the hadronic calorimeter which are as well within the inner magnet system as shown in Figure 3.5.

The electromagnetic calorimeter

The electromagnetic calorimeter is designed to detect elecromagnetic particle showers produced by electrons, positrons or photons decaying into electron positron pairs (pair production). It is composed of alternating layers of "passive" material (liquid argon) where the energy of a particle gets absorbed and "active" material (lead) where the particle showers are produced. An electromagnetic particle shower is a cascade of secondary particles originating from a high energy electron, positron or photon interacting with matter. For low energy particles, ionization and compton scattering are the dominating

processes while for energies larger than ~10 MeV, photons and electrons/positrons mostly interact via pair production and Bremsstrahlung, respectively. Bremsstrahlung is electromagnetic radiation a charged particle emits when it is accelerated by interaction with another charged particle, typically an atomic nucleus. When a high energy electron/positron enters the active layer of the calorimeter it emits photons through Bremsstrahlung with sufficiently high energies that those photons are able to produce electron positron pairs which again radiate Bremsstrahlung and therefore produce more secondary particles. These processes take place repeatedly resulting in a so called particle shower. The deposited energy can be measured and even information about the direction is taken by the calorimeter as the readout is separated into thin η and ϕ stripes [16]. The calorimeter is structured in a concentric cylinder along the beam line (the barrel), disks centered at the beamline (end-caps) and a forward calorimeter, combined covering a solid angle of nearly 4π [17].

The hadronic calorimeter

The hadronic calorimeter is based on the same principle of alternating layers as the electromagnetic calorimeter but the effects leading to the shower development are quite different. Whereas for the electromagnetic shower the Bremsstrahlung is the dominant effect, hadronic showers develop through successive inelastic hadronic interaction where the dominant processes are multiparticle production and particle emission from excited nuclei. The secondary particles scatter inelastically as well until they fall below the pion production threshold which are the lightest mesons [18].
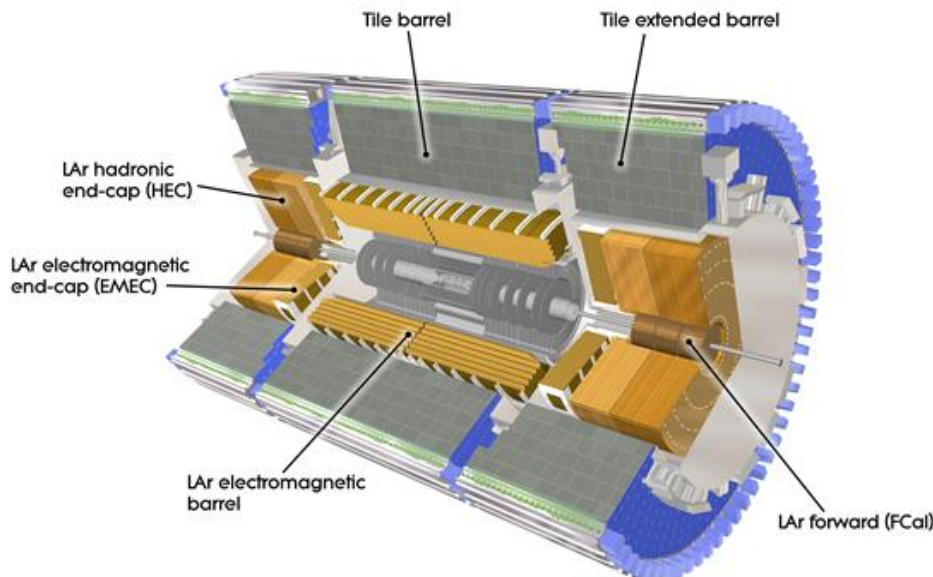

Figure 3.5: The electromagnetic and hadronic calorimeter are illustrated. The electromagnetic calorimeter, wrapped around the inner detector, is displayed in a yellow/brown color, the outer parts colored in grey and blue show the hadronic calorimeter [19].

3.2.3 The muon spectrometer

The muon spectrometer is the outermost part of the ATLAS detector and combined with the magnet system mainly responsible for its enormous dimensions. The muons pass the inner layers of the detector almost unaffected until they reach the spectrometer. Using superconducting magnetic coils, a strong magnetic field is generated to deflect the muons. There are 1 150 muon drift tube chambers which each consist of several drift tubes, filled with a gas mixture of argon and carbon dioxide, and a central wire with a high voltage between wire and tube wall. The entering muons each leave a track in the drift chambers as they ionize the atoms which then results in electromagnetic showers registered as electronic signals.

Jet reconstruction

Jets consist of numerous objects making it difficult to distinguish between objects being part of the jet and objects from underlying events which are referred to as pile up. In this chapter, two jet collection procedures and the jet reconstruction algorithm used at ATLAS are briefly introduced.

4.1 Jet collections

The jets used in this thesis are obtained with the Particle Flow (PFlow) collection but since it is based on formations of TopoClusters both are described in the following sections.

4.1.1 TopoCluster

The aim of the TopoCluster jet collection is to merge topologically connected regions of the calorimeter which detect a signal. Therefore, the calorimeter is divided into small units (cells) and for each cell the signal to noise ratio $\frac{S}{N}$ is determined where the noise N accounts for electronic noise and pile up. The first step is to look for seed cells with a local maximum of $\frac{S}{N}$ above a certain threshold which is set to 4 in the ATLAS experiment. In the second step, the neighboring cells are inspected and are added to the cluster if the absolute energy measured in those cells exceeds a second threshold of $\frac{S}{N} > 2$. This step is repeated iteratively until all neighboring cells passing this criterion are merged to the so called protocluster. In a final step, all cells neighboring this protocluster are added to form a TopoCluster. If one TopoCluster contains multiple local maxima, it is split until every cluster has only one local maximum to gain more detailed information about the jets substructure. A simulation of the TopoCluster collection algorithm is illustrated in Figure 4.1, a more detailed description can be found in reference [20].

4.1.2 ParticleFlow

The ParticleFlow algorithm uses tracking information, additionally to the TopoClusters, because at low transverse momenta the tracking detectors show a better resolution than the calorimeters [21]. To avoid double counting, the energy a charged particle deposited in the calorimeter has to be removed from the TopoCluster. The first step is to match tracks and clusters which is not trivial, because the energy of one particle can be deposited in more than one TopoCluster. The algorithm evaluates the probability for this for every matched track and cluster and then decides to either add another cluster to the track or to leave this set when it is considered to be complete. For calculating the expected energy deposit of a particle with respect to its momentum $\left\langle E_{\mathrm{dep}} \right\rangle = p^{\mathrm{track}} \left\langle E_{\mathrm{ref}}^{\mathrm{clus}} / p_{\mathrm{ref}}^{\mathrm{track}} \right\rangle$, the average response has to be determined.
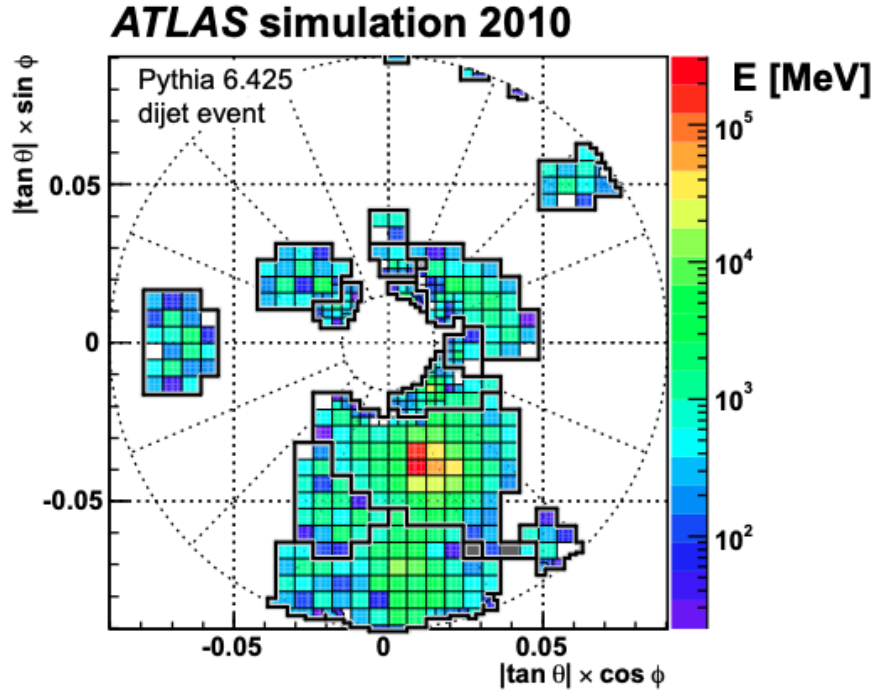
Figure 4.1: Cells clustered with the TopoCluster algorithm are shown. The color indicates the amount of deposited energy in the corresponding cell. The thicker black lines depict the borders of one cluster [20].

This is done using single particle samples with no contribution from pile up. Then, the energy is removed cell by cell from the matched cluster or set of clusters. If the remnant energy is consistent with energy fluctuations of a single particle shower it is removed entirely. In Figure 4.2 this process is schematically shown for four combinations of number of particles and number of TopoClusters. The output from the PFlow algorithm consists of tracks, modified clusters and unmodified clusters which were not matched to a track and therefore no energy has been removed. Further information can be found in reference [21].

4.2 Jet reconstruction algorithms

The jets used in this thesis are reconstructed using the anti-k_t algorithm which is a sequential recombination algorithm. It calculates the distance between two objects i and j, and merges them if their distance lies beneath a chosen threshold. The definition of the distance is a distinctive feature of a jet reconstruction algorithm. A general definition is

$$d_{ij} = \min\left(p_{T,i}^{2p}, p_{T,j}^{2p}\right) \frac{\Delta R_{ij}^2}{R^2} \tag{4.1}$$

where R is a radius parameter which is set to 0.4 for small-R jets and 1 for large-R jets at ATLAS. The parameter p is set to -1 in the anti-k_t algorithm, in other algorithms like the k_t algorithm or the Cambridge/Aachen algorithm it is set to $p = 1$ and $p = 0$, respectively [22]. Defining the distance with
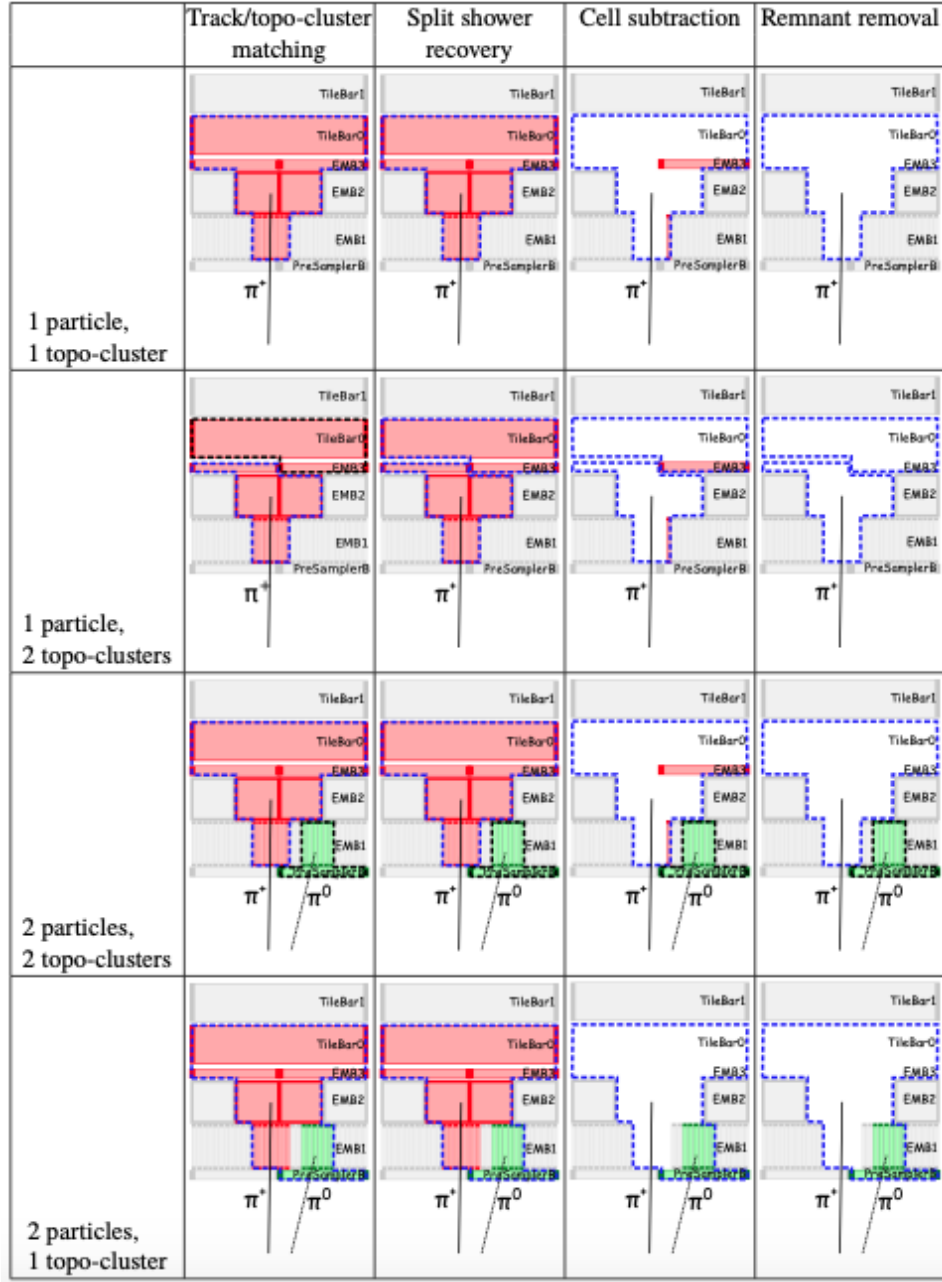
Figure 4.2: Four different examples are sketched to show how the PFlow algorithm operates. Three layers of the electromagnetic calorimeter EMB1, EMB2 and EMB3 and the first two of the hadronic calorimeter TileBar0 and TileBar1 are shown. The blue dotted lines depict the boundaries of TopoClusters which are filled by red colored cells representing the energy deposited by a charged particle e.g. π^+ and green colored cells representing energy deposited by a neutral particle e.g. π^0. The tracks of the particles are shown as black continous lines [21].

$p < 0$ in consequence assigns small distances when at least one of the particles is a hard[1] particle. This leads to soft particles rather clustering with hard particles than combining among themselves, resulting in circular shaped hard jets not distorted by near soft jets as can be seen in Figure 4.3. This recombination process takes place successively until all particles within the chosen threshold are merged [23].
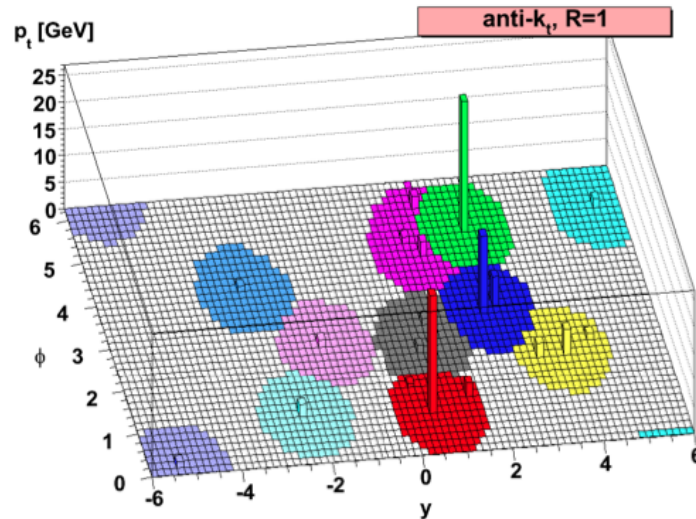

Figure 4.3: A multijet event reconstructed with the anti-k$_t$ algorithm with R = 1 in the $\eta - \phi$-plane where the η-axis corresponds to the y-axis in this figure. Three hard jets in blue, green and red and multiple soft jets can be seen [23].

4.3 Monte Carlo simulations

A widely used tool in particle physics to obtain and validate results are Monte Carlo (MC) simulations. Simplified, they imitate particle collisions and the following events based on probabilities and pseudo random decisions [24].

The process of data taking at ATLAS can be sectioned into five steps. Those are:

- the event itself

- the showering behavior which describes the production of secondary particles immediately after the event

- the measurement which leads to smearing and a loss of information due to the limited resolution of the detector

- the reconstruction which was explained in detail in this chapter

- the calibration which maps the detector output to values with a physical meaning

---

[1] Hard and soft, in this context, is used equivalent to "corresponding to a high momentum" and "corresponding to a low momentum", respectively.

With MC generators, the first three steps are simulated, the reconstruction and calibration is performed as it is on real data. If each step is executed, the jets are called reconstructed (reco) jets. Skipping the measurement and calibration yields the so called truth jets where no detector or calibration effects cause any smearing in the momentum distributions [25].

The two MC generators used in this thesis are Pythia8 and Sherpa, detailed information can be found in reference [26] and [27], respectively.

Jet energy resolution

5.1 Contributions

Fluctuations in the jet energy can result either from physical effects or from calibration and detector effects. The term jet energy resolution (JER) is defined as

$$\text{JER} = \frac{\sigma(p_{\text{T}})}{p_{\text{T}}} \tag{5.1}$$

with p_{T} the jets momentum in the transverse plane (the x-y-plane) referred to as transverse momentum and $\sigma(p_{\text{T}})$ the width of its distribution. It should only be associated with detector uncertainties, the other contributions are supposed to be separated.

Those other contributions are mainly initial state radiation (ISR), final state radiation (FSR) and so called out-of-cone effects[1] (OOC effects) which describe smearing due to particles which were wrongly considered not to be part of the jet or particles included by the jet algorithm which, originally, were not associated with the jet. Initial and final state radiation describe gluons radiated away before and after the collision, respectively.

The JER, as a calorimeterbased resolution, can be parameterized by three terms: a noise term $N \sim \frac{1}{p_{\text{T}}}$, a stochastic term $S \sim \frac{1}{\sqrt{p_{\text{T}}}}$ and a constant term C accounting for pile up, intrinsic fluctuations of the shower development (which can be assumed to be poisson distributed) and energy loss due to dead material or gaps in the calorimeter, respectively [28].

5.2 Measurement methods

This thesis only focuses on measurement methods in dijet events, however, for the sake of completeness it should be mentioned are other methods which exploit the conservation of transverse momentum in events with a jet and a Z boson or a photon [29].

---

[1] The name originates from earlier used iterative cone reconstruction algorithms which are explained in more detail in reference [22].

5.2.1 Dijet balance

The JER as a function of pseudorapidity η and the average transverse momentum of a dijet event

$$p_{\mathrm{T,avg}} = \frac{p_{\mathrm{T},1} + p_{\mathrm{T},2}}{2}, \tag{5.2}$$

with $p_{\mathrm{T},1}$ and $p_{\mathrm{T},2}$ the transverse momenta of both jets, can be obtained using the asymmetry of dijet events which is quantified as

$$\mathcal{A} = \frac{p_{\mathrm{T}}^{\mathrm{probe}} - p_{\mathrm{T}}^{\mathrm{ref}}}{p_{\mathrm{T,avg}}} \tag{5.3}$$

where probe and reference denote different η-regions of the detector. The probe region is the one to be investigated and as reference region one with high statistics and a presumably high resolution should be selected. The width of the asymmetry distribution then can be decomposed into the quadratic sum (symbolized as $\oplus$) of the average jet energy resolutions of both regions.

$$\sigma\left(\mathcal{A}\right) = \frac{\sigma\left(p_{\mathrm{T}}^{\mathrm{ref}}\right) \oplus \sigma\left(p_{\mathrm{T}}^{\mathrm{probe}}\right)}{p_{\mathrm{T,avg}}} \tag{5.4}$$

$$= \left\langle \frac{\sigma\left(p_{\mathrm{T}}\right)}{p_{\mathrm{T}}} \right\rangle_{\mathrm{ref}} \oplus \left\langle \frac{\sigma\left(p_{\mathrm{T}}\right)}{p_{\mathrm{T}}} \right\rangle_{\mathrm{probe}} \tag{5.5}$$

where for the second equality $\left\langle p_{\mathrm{T}}^{\mathrm{probe}} \right\rangle = \left\langle p_{\mathrm{T}}^{\mathrm{ref}} \right\rangle = \left\langle p_{\mathrm{T,avg}} \right\rangle = \left\langle p_{\mathrm{T}} \right\rangle$ is assumed. For events with both jets within the reference region, Equation 5.5 simplifies to

$$\left\langle \frac{\sigma\left(p_{\mathrm{T}}\right)}{p_{\mathrm{T}}} \right\rangle_{\mathrm{ref}} = \frac{\sigma\left(\mathcal{A}\right)}{\sqrt{2}}. \tag{5.6}$$

Fitting a Gaussian to the asymmetry distribution, the resolution of the reference region can be determined. By substituting this result in Equation 5.5, the JER of further regions can be calculated.

The derived resolution which is associated with effects due to physics (ISR and FSR), reconstruction (OOC) and detector uncertainties is referred to as "detector level" JER. The resolution accounting for physical effects exclusively is called "particle level" JER.

To eliminate contributions from not detector related effects, e.g. ISR, FSR and OOC effects, a particle level correction[2] is necessary. Therefore, the JER of the truth jets is calculated with the same procedure and subtracted in quadrature from the data or reconstructed jet resolutions as described in Equation 5.7 [25].

$$\sigma_{p_{\mathrm{T}}} = \sqrt{\left(\sigma_{p_{\mathrm{T}}}\right)_{\mathrm{reco}}^{2} - \left(\sigma_{p_{\mathrm{T}}}\right)_{\mathrm{truth}}^{2}} \tag{5.7}$$

with $\frac{\sigma(p_{\mathrm{T}})}{p_{\mathrm{T}}}$ denoted as $\sigma_{p_{\mathrm{T}}}$ for reasons of readability.

The disadvantage of this particle level correction via quadratic subtraction is that the resulting statistical error estimated by gaussian error propagation tends to get scaled up for $\sigma_{p_{\mathrm{T}}}$ smaller than order unity as

---

[2] The name "particle level correction" is used due to the fact that this correction compares to particle level. It is applied, however, on detector level which easily leads to confusion.

shown in the following equations:

$$\Delta\sigma_{p_\mathrm{T}} = \sqrt{\left(\frac{\mathrm{d}\sigma_{p_\mathrm{T}}}{\mathrm{d}\left(\sigma_{p_\mathrm{T}}\right)_\mathrm{reco}} \cdot \Delta\left(\sigma_{p_\mathrm{T}}\right)_\mathrm{reco}\right)^2 + \left(\frac{\mathrm{d}\sigma_{p_\mathrm{T}}}{\mathrm{d}\left(\sigma_{p_\mathrm{T}}\right)_\mathrm{truth}} \cdot \Delta\left(\sigma_{p_\mathrm{T}}\right)_\mathrm{truth}\right)^2} \tag{5.8}$$

$$= \frac{\sqrt{\left(\sigma_{p_\mathrm{T}} \cdot \Delta\sigma_{p_\mathrm{T}}\right)^2_\mathrm{reco} + \left(\sigma_{p_\mathrm{T}} \cdot \Delta\sigma_{p_\mathrm{T}}\right)^2_\mathrm{truth}}}{\sigma_{p_\mathrm{T}}} \tag{5.9}$$

Another concern regarding this method of deriving the JER is its strong dependence on Monte Carlo simulations as the correction for physical effects is solely based on MC generated truth jets. The latest results from the ATLAS collaboration determining the JER using the dijet balance method on run 2 data can be found in reference [30].

5.2.2 Bisector method

A more data driven approach to determine the JER is the bisector method which is based on geometrical considerations of dijet events [31]. The coordinate system used is shown in Figure 5.1 where $\vec{p}_{\mathrm{T},1}$ and $\vec{p}_{\mathrm{T},2}$ correspond to the transverse momenta of the two jets. If both jets are located within the same η region, they are randomly assigned, and in case of one jet in the central region (reference, $0.2 < \eta < 0.7$) and one in an outer (probe) region of the detector, the probe jet is tagged as jet 1. The α-axis bisects the angle $\Delta\phi_{12}$ between the two momentum vectors and the β-axis is chosen perpendicular to it such that the β component of jet 1 is positive and the coordinate system is right-handed. The object of interest is the imbalance vector $\vec{p}_{\mathrm{T,add}} = \vec{p}_{\mathrm{T},1} + \vec{p}_{\mathrm{T},2}$ and its projections $\vec{p}_\alpha$ and $\vec{p}_\beta$ onto the respective axis with

$$p_\alpha = p_\mathrm{T,add}\cos(\gamma) \tag{5.10}$$

$$p_\beta = p_\mathrm{T,add}\sin(\gamma) \tag{5.11}$$

where γ equals the angle between the imbalance vector and the α-axis. In the following equations, detector and particle level are distinguished and denoted as D and P, respectively.

For a perfectly well balanced dijet event the absolute value of the unbalance vector $p_\mathrm{T,add}$ should be equal to zero. However, as discussed in the previous section, there are multiple sources which lead to non zero p_α and p_β components.

The ISR is assumed to be isotropic in the transverse plane since there is no preferred direction of colorflow previous to the collision, i.e. the contributions to the width of p_α and p_β on particle level should be approximately equal, yielding

$$\left(\sigma_\alpha^2\right)^\mathrm{P} \approx \left(\sigma_\beta^2\right)^\mathrm{P}. \tag{5.12}$$

The validity of this assumption was verified by looking at the standard deviations σ_α^D, σ_β^D and $\left[\left(\sigma_\beta^2 - \sigma_\alpha^2\right)^\mathrm{D}\right]^{1/2}$ for an increasing cut on a possible third jet thus a growing contribution from soft radiation. As expected, the standard deviations increased with the cut whereas the square root of the difference between their variances remained constant within statistical fluctuations. In the final analysis, the precision of this assumption was accommodated as a systematic uncertainty [31].

The OOC and detector effects are distributed mainly along the dijet axis meaning they contribute almost exclusively to the width of the p_β distribution due to the fact that those mostly change the length of $\vec{p}_{\mathrm{T},1}$ and $\vec{p}_{\mathrm{T},2}$ but not their direction. Classifying the impact of FSR in such a way is quite difficult as it
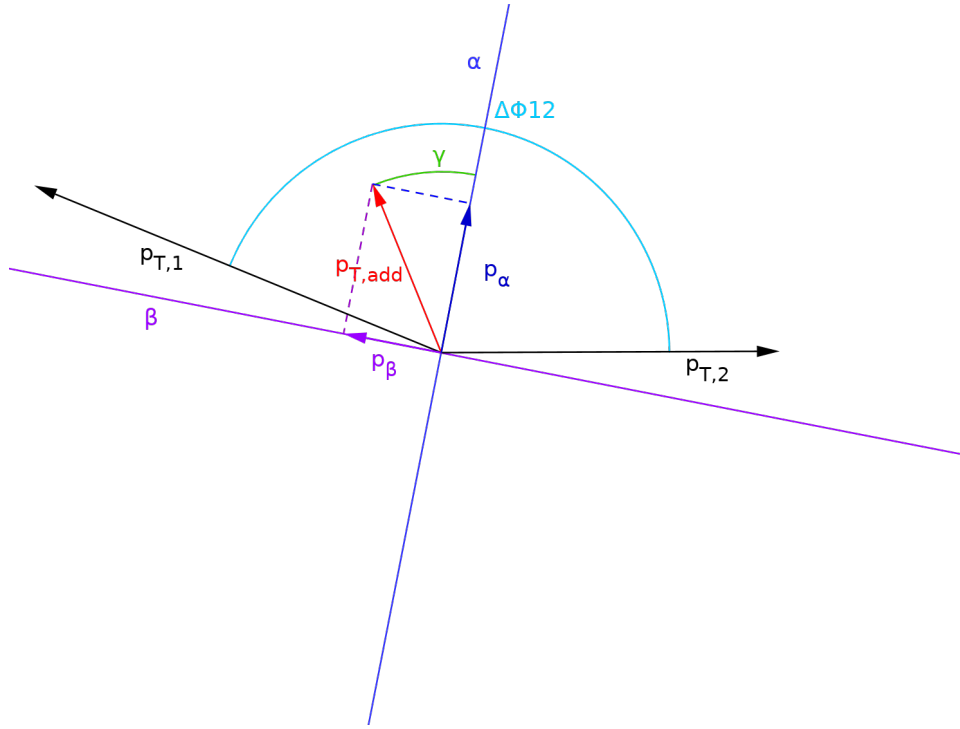
Figure 5.1: The bisector coordinate system with the α-axis bisecting the angle $\Delta\phi_{12}$ between $\vec{p}_{\mathrm{T},1}$ and $\vec{p}_{\mathrm{T},2}$, the transverse momenta of the two jets, and the β-axis perpendicular to it. The imbalance vector $\vec{p}_{\mathrm{T,add}} = \vec{p}_{\mathrm{T},1} + \vec{p}_{\mathrm{T},2}$ is shown in red and its projections onto the α- and β-axis in blue and purple, respectively [32].

is neither isotropically distributed nor limited to solely contributing to only p_α or p_β. However, the main fraction of FSR should be directed along the β-axis since this is the preferred direction of colorflow after the collision. The remaining contribution in other directions can be assumed negligible as Equation 5.12 is valid.

In conclusion, the width of the p_α truth and reco distributions are associated with ISR, the width of p_β truth with ISR, FSR and OOC and p_β reco with ISR, FSR, OOC and detector uncertainties. Since the contribution of FSR is small compared to OOC effects it is often neglected to be mentioned.

To extract only the detector related resolution, the width of the β-component of the imbalance vector can be decomposed into three terms

$$p_\beta^{\mathrm{D}} = p_{1,\beta}^{\mathrm{D}} - p_{2,\beta}^{\mathrm{D}} \tag{5.13}$$

$$= \left(p_{1,\beta}^{\mathrm{D}} - p_{1,\beta}^{\mathrm{P}}\right) - \left(p_{2,\beta}^{\mathrm{D}} - p_{2,\beta}^{\mathrm{P}}\right) + \left(p_{1,\beta}^{\mathrm{P}} - p_{2,\beta}^{\mathrm{P}}\right) \tag{5.14}$$

where the first two terms and the last term account for detector contributions and particle level imbalances, respectively.

Assuming $\Delta\phi_{12}^{\mathrm{D}} = \Delta\phi_{12}^{\mathrm{P}} = \Delta\phi_{12}$ the following relations can be derived:

$$\mathrm{Var}\left(p_{\beta}^{\mathrm{D}}\right) = \left(\sigma_{\beta}^{2}\right)^{\mathrm{D}} \tag{5.15}$$

$$\mathrm{Var}\left(p_{1,\beta}^{\mathrm{P}} - p_{2,\beta}^{\mathrm{P}}\right) = \left(\sigma_{\beta}^{2}\right)^{\mathrm{P}} \tag{5.16}$$

$$\mathrm{Var}\left(p_{1,\beta}^{\mathrm{D}} - p_{1,\beta}^{\mathrm{P}}\right) = \mathrm{Var}\left[\left(p_{\mathrm{T},1}^{\mathrm{D}} - p_{\mathrm{T},1}^{\mathrm{P}}\right)\cos\left(\frac{\pi}{2} - \frac{\Delta\phi_{12}}{2}\right)\right] \tag{5.17}$$

$$= \mathrm{Var}\left[\left(p_{\mathrm{T},1}^{\mathrm{D}} - p_{\mathrm{T},1}^{\mathrm{P}}\right)\sin\left(\frac{\Delta\phi_{12}}{2}\right)\right] \tag{5.18}$$

$$\simeq \sigma_{1}^{2}\left(p_{\mathrm{T}}\right)\left\langle\sin^{2}\left(\frac{\Delta\phi_{12}}{2}\right)\right\rangle \tag{5.19}$$

$$\mathrm{Var}\left(p_{2,\beta}^{\mathrm{D}} - p_{2,\beta}^{\mathrm{P}}\right) \simeq \sigma_{2}^{2}\left(p_{\mathrm{T}}\right)\left\langle\sin^{2}\left(\frac{\Delta\phi_{12}}{2}\right)\right\rangle \tag{5.20}$$

If both jets are located in the same η-region, i.e. $\sigma_{1}^{2}\left(p_{\mathrm{T}}\right) = \sigma_{2}^{2}\left(p_{\mathrm{T}}\right) = \sigma^{2}\left(p_{\mathrm{T}}\right)$, Equation 5.14 yields

$$\left(\sigma_{\beta}^{2}\right)^{\mathrm{D}} \simeq 2\sigma^{2}\left(p_{\mathrm{T}}\right)\left\langle\sin^{2}\left(\frac{\Delta\phi_{12}}{2}\right)\right\rangle + \left(\sigma_{\beta}^{2}\right)^{\mathrm{P}}. \tag{5.21}$$

The analogues procedure for the α-component yields

$$\left(\sigma_{\alpha}^{2}\right)^{\mathrm{D}} \simeq 2\sigma^{2}\left(p_{\mathrm{T}}\right)\left\langle\cos^{2}\left(\frac{\Delta\phi_{12}}{2}\right)\right\rangle + \left(\sigma_{\alpha}^{2}\right)^{\mathrm{P}}. \tag{5.22}$$

Subtracting Equation 5.21 from 5.22 and using Equation 5.12 yields

$$\frac{\sigma\left(p_{\mathrm{T}}\right)}{p_{\mathrm{T}}} \simeq \sqrt{\frac{\left(\sigma_{\beta}^{2}\right)^{\mathrm{D}} - \left(\sigma_{\alpha}^{2}\right)^{\mathrm{D}}}{2p_{\mathrm{T}}^{2}\langle\|\cos\Delta\phi_{12}\|\rangle}}. \tag{5.23}$$

For two jets in different η-regions this formula changes to

$$\frac{\sigma_{1}\left(p_{\mathrm{T}}\right)}{p_{\mathrm{T}}} \simeq \sqrt{\frac{\left(\sigma_{\beta}^{2}\right)^{\mathrm{D}} - \left(\sigma_{\alpha}^{2}\right)^{\mathrm{D}}}{p_{\mathrm{T}}^{2}\langle\|\cos\Delta\phi_{12}\|\rangle} - \frac{\sigma_{2}^{2}\left(p_{\mathrm{T}}\right)}{p_{\mathrm{T}}^{2}}} \tag{5.24}$$

where the second term inside the square root is the JER of the second region (reference region) which has to be determined using Equation 5.23.

The JER derived by this approach is already corrected for ISR effects by subtracting the variance of the p_{α} distribution from the one of the p_{β} distribution. Still, a particle level correction needs to be applied, as explained in Section 5.2.1, since the result given by this formula accounts for both detector and OOC uncertainties. To bypass this correction entirely, the term $\left(\sigma_{\beta}^{2}\right)^{\mathrm{D}} - \left(\sigma_{\alpha}^{2}\right)^{\mathrm{D}}$ must not include a contribution from OOC effects. A possible approach to achieve this is presented in the next chapter.

Implementation of the bisector method

6.1 Event selection

In this thesis, dijet and multijet events from data obtained in proton-proton collisions at the ATLAS experiment in 2017 with an integrated luminosity of $\mathcal{L} = 46.9\,\text{fb}^{-1}$ [33] are used as well as MC simulated samples with two different generators, namely, Pythia8 and Sherpa. The applied good run list and production tags of data and MC can be found in Appendix A along with information on the event selection. For the MC Pythia8 sample, three different dijet selections (tight, nominal and loose) have been analyzed which differ on the cuts for the transverse momentum of a possible third jet $p_{\text{T},3}$ and the angle $\Delta\phi_{12}$ that separates jet 1 and jet 2. The exact values are listed in Table 6.1. Comparisons of

Dijet selection	tight	nominal	loose
$N_{\text{tracks, PV}}$	≥ 2	≥ 2	≥ 2
N_{jets}	≥ 2	≥ 2	≥ 2
$p_{\text{T},3}$	$\leq 0.2 p_{\text{T,avg}} \vee \leq 20\,\text{GeV}$	$\leq 0.25 p_{\text{T,avg}} \vee \leq 25\,\text{GeV}$	$\leq 0.3 p_{\text{T,avg}} \vee \leq 30\,\text{GeV}$
$\Delta\phi_{12}$	≥ 2.5	≥ 2.7	≥ 2.9

Table 6.1: The cuts for the three different dijet selections used in this thesis are shown. $N_{\text{tracks, PV}}$, N_{jets} and $p_{\text{T},3}$ correspond to the number of tracks originating from the primary vertex, the number of jets and the transverse momentum of a possible third jet, respectively.

data and MC Pythia8 distributions are displayed in Figure 6.1(a) and 6.1(b) for $p_{\text{T,avg}}$ and the cosine of $\Delta\phi_{12}$, and in Figure 6.2(a) and 6.2(b) for p_α and p_β, respectively. In all plots data and MC show good agreement within statistical uncertainties, except for the low $p_{\text{T,avg}}$ region in Figure 6.1(a) where a trend towards less events in the data sample than the MC Pythia8 sample can be observed. Comparing the Sherpa generated events to data shows bigger fluctuations as displayed exemplary in Figure 6.3 which was expected since the sherpa sample has less statistics by a factor of ~ 10. Therefore, this thesis is mainly focused on the MC Pythia8 sample. Additional plots showing comparisons of Sherpa and data can be found in Appendix B. The used $p_{\text{T,avg}}$ and $|\eta|$ binning is specified in Table 6.2.

6.2 The fitting procedure

In order to calculate the JER, according to Equation 5.23, three parts have to be determined separately. For the p_{T} value the average (RMS) of the p_{T} bin to be investigated is calculated. The mean of the cosine

(a)

(b)
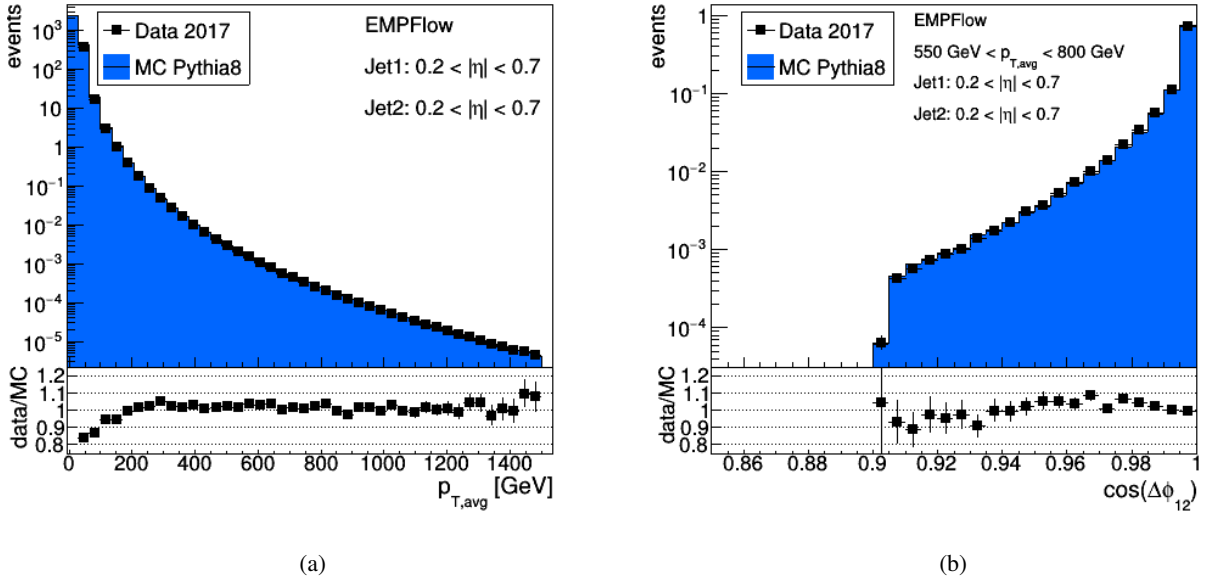
Figure 6.1: A comparison of data and MC Pythia8 is shown for $p_{\mathrm{T,avg}}$ (a) and $\cos(\Delta\phi_{12})$ (b).
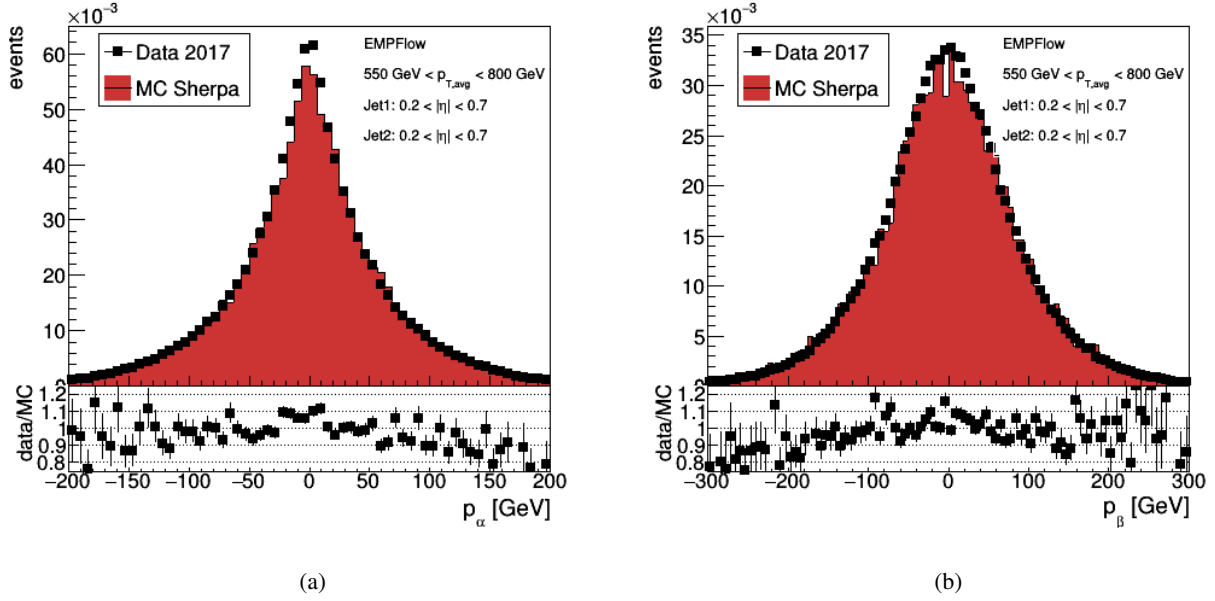

(a)

(b)
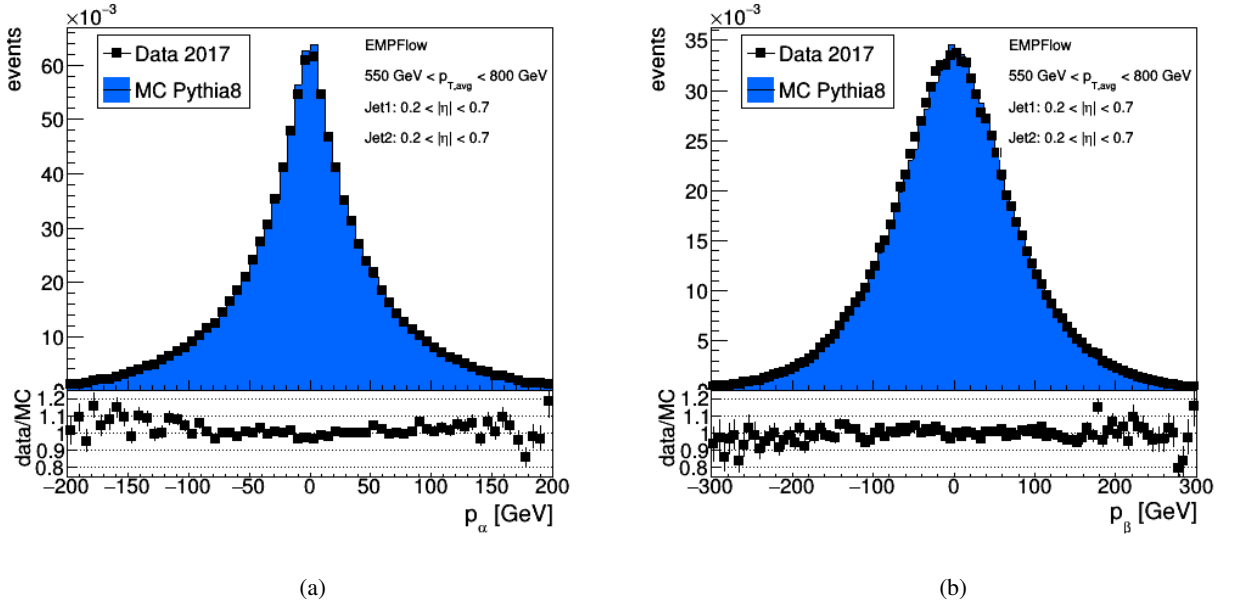
Figure 6.2: A comparison of data and MC Pythia8 is shown of an exemplary p_α distribution (a) and p_β distribution (b) with both jets in the reference region ($0.2 < |\eta| < 0.7$) and $550\,\mathrm{GeV} < p_{\mathrm{T,avg}} < 800\,\mathrm{GeV}$.

$p_{\mathrm{T,avg}}$ [GeV]	30	40	55	80	110	150	200	300	400	550	800	1100	1500
$|\eta|$	0.0	0.2	0.7	1.0	1.3	1.8	2.5	2.8	3.2	3.5	4.5		

Table 6.2: The binning of the $p_{\mathrm{T,avg}}$ and $|\eta|$ regions the JER is calculated for is shown.

(a)   (b)

Figure 6.3: comparison of data and MC Sherpa is shown of an exemplary p_α distribution (a) and p_β distribution (b) with both jets in the reference region ($0.2 < |\eta| < 0.7$) and $550\,\text{GeV} < p_{\text{T,avg}} < 800\,\text{GeV}$

distribution of the azimuthal angle $\Delta\phi_{12}$ is determined in the same way. Not as trivial, though, is the $\left(\sigma_\beta^2\right)^{\text{D}} - \left(\sigma_\alpha^2\right)^{\text{D}}$ part. The default approach would be to fit the p_α and p_β distribution as Gaussians

$$g(x) = C \exp\left[-\frac{1}{2}\left(\frac{x-\mu}{\sigma}\right)^2\right] \tag{6.1}$$

with σ the standard deviation, μ the center of the peak and C a normalization variable. This allows to easily subtract their variances which are defined as the standard deviation squared. Looking at the p_α distribution in Figure 6.4(a) which is fitted with a Gaussian function indicates this is not going to work well as it decreases rather exponentially than quadratically. Fitting an exponential function

$$f(x) = \exp\left[a \cdot |x|^b + c\right] \tag{6.2}$$

to this distribution results in a significant improvement of the fit, as displayed in Figure 6.4(b), but is accompanied by a new problem. Subtracting the width of an exponential from a Gaussian requires a consistent definition of the width for both functions which does not exist. The solution to this is a convolution of both functions which was first introduced in the analysis of run 2 [32]. A more detailed explanation is given in the following sections.

6.3 Basic convolution method

A convolution of two functions $f(x)$ and $g(x)$ is defined as follows:

$$f(x) \circledast g(x) = (f \circledast g)(x) \equiv \int_{\mathbb{R}^n} f(\tau)g(x-\tau)\mathrm{d}\tau.$$

(a)   (b)
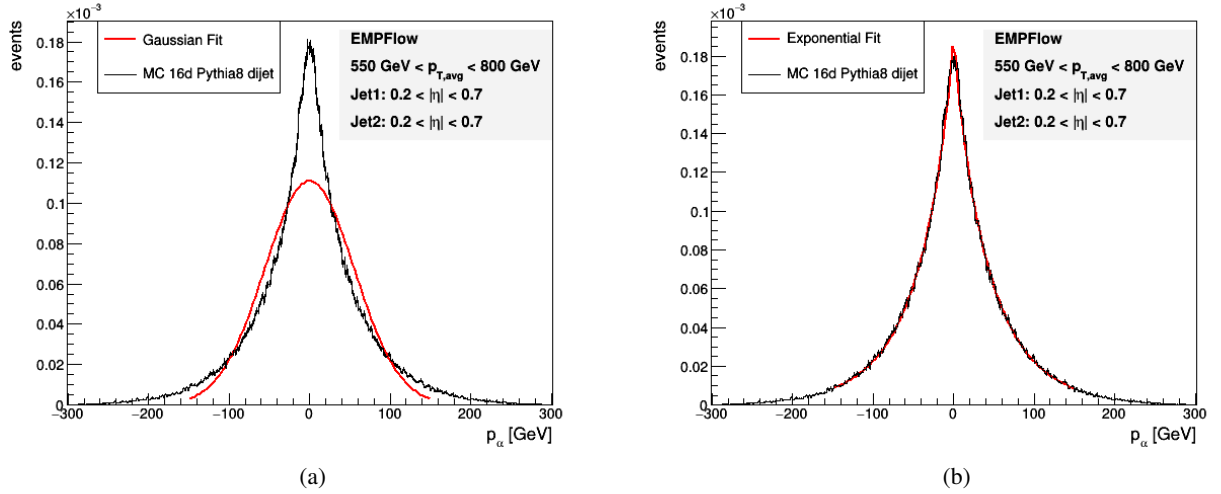
Figure 6.4: an exemplary p_α distribution fitted with a Gaussian function (a) and an exponential function (b) with both jets in the reference region ($0.2 < |\eta| < 0.7$) and $550\,\text{GeV} < p_{\text{T,avg}} < 800\,\text{GeV}$.

The resulting function describes how the shape of $f(x)$ is modified by $g(x)$. This allows to avoid the subtraction of variances but to determine the width of the p_β distribution excluding the contribution from the p_α uncertainty. The idea is to:

- fit both p_α distributions (truth and reconstructed) with an exponential function and fix the parameters

- fit both p_β distributions (truth and reconstructed) with a convolution of the exponential function with fixed parameters from the respective previous p_α fit and a Gaussian function with floating parameters

- use the variance of the convoluted Gaussian function as $\left(\sigma_\beta^2\right)^{\text{D}} - \left(\sigma_\alpha^2\right)^{\text{D}}$

- calculate the JER for truth and reco level and apply the particle level correction, i.e. subtract the truth JER from the reco JER in quadrature for the final result

The advantage of this procedure, compared to the dijet balance method, is that the ISR uncertainties are taken into account from the reconstructed p_α distributions which reduces the impact of MC simulations. However, there is still room for improvement. For one thing, the impact of the quadratic subtraction is reduced but the aim would be to avoid it entirely, secondly, the p_β^{truth} distribution may be modeled better with this method but even the convolution does not seem to be a suitable function as shown in Figure 6.5.

6.4 Advanced convolution method

Since the p_β^{truth} distribution seems to decrease even steeper than a convolution of a Gaussian and an exponential function, the next step is a convolution of two exponentials. The second change of this method is to abandon the particle level correction via quadratic subtraction but instead convolute a second time, i.e. the OOC effects are now as well taken into account by convoluting. The step by step plan looks as follows:
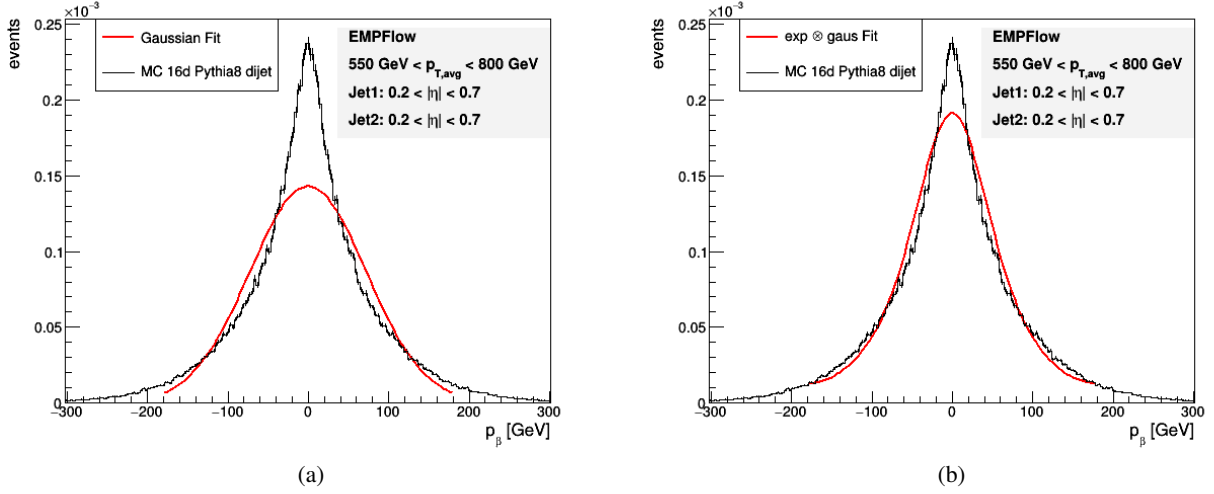
Figure 6.5: A p_β^{truth} distribution fitted with a Gaussian (a) and a convolution of an exponential function and a Gaussian (b).

- fit both p_α distributions with an exponential function and fix the parameters

- fit the p_β^{truth} distribution with a convolution of the exponential with fixed parameters from the p_α^{truth} fit and a second exponential with floating parameters

- fit the p_β^{reco} distribution with a convolution of the exponential from the p_α^{reco} fit and the second exponential from the p_β^{truth} fit with fixed parameters and a Gaussian with floating parameters

- use the variance of the convoluted Gaussian as $\left(\sigma_\beta^2\right)^{\text{D}} - \left(\sigma_\alpha^2\right)^{\text{D}}$ and calculate the JER

The width of this final Gaussian is only associated with detector effects making the particle level correction redundant. Figure 6.6 shows the same p_β^{truth} distribution as in Figure 6.5 but modeled with a convolution of two exponential functions according to this method. Comparing both figures confirms that the modified fitting procedure is in fact favorable. In Figure 6.7 one full performance of the advanced convolution method procedure is displayed for one $p_{\text{T,avg}}$ bin in the reference region, a similar plot for an outer pseudorapidity region can be found in Appendix C. To determine the JER in other η regions, there are two possible strategies.

The first would be to use dijet events with both jets within the same η region and calculate the JER according to Equation 5.23.

The second strategy designates a reference region and dijet events with one jet located in the reference region and one in the η region being probed are analyzed. To calculate the JER, the resolution of the reference region must be known. Therefore, in this region the first strategy has to be applied.

The decision which strategy to follow was made in favor of the second one because it showed higher statistics. Further, the symmetry of the ATLAS detector allows to assume that the JER of a pseudorapidity region $\eta_1 < \eta_{\text{probe}} < \eta_2$ will be equal to the JER of $-\eta_2 < \eta_{\text{probe}} < -\eta_1$. Thereby, the absolute values of η can be used enhancing the statistics even more.

29
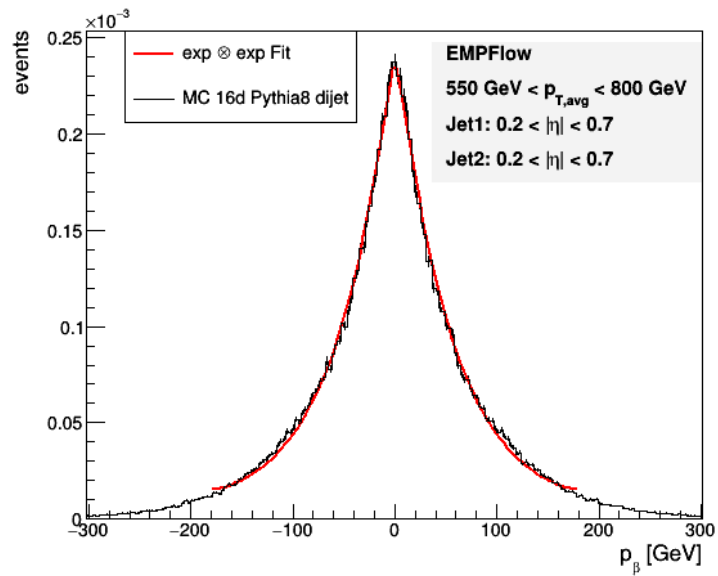
Figure 6.6: The p_β^{truth} distribution from the previous plots shown in Figure 6.5 modeled with a convolution of two exponential functions according to the advanced convolution method.
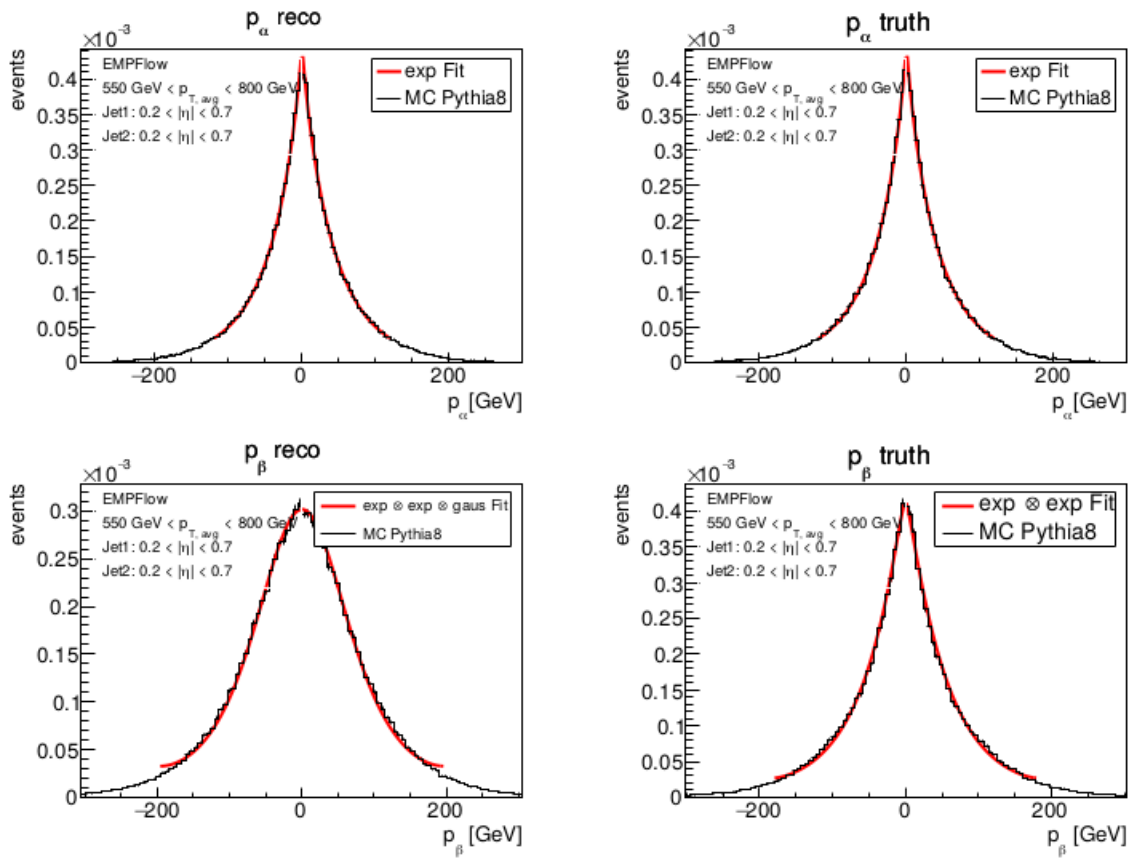
Figure 6.7: One full performance of the advanced convolution method is shown for $550\,\text{GeV} < p_{\text{T,avg}} < 800\,\text{GeV}$ and both jets located in the reference region ($0.2 < |\eta| < 0.7$). The distributions are simulated with the MC generator Pythia8.

Results

The JER obtained with this new advanced fitting method is presented in p_T and η dependence. It is compared for three MC Pythia8 dijet selections (tight, nominal and loose) with different cuts for the transverse momentum of a possible third jet and the azimuthal angle $\Delta\phi_{12}$. Secondly, a comparison of the JER obtained from data and the two MC generators Pythia8 and Sherpa is shown and discussed. Previous results, published in 2019 by the ATLAS collaboration for data recorded in 2012 at $\sqrt{s} = 8\,\mathrm{TeV}$, are displayed in Figure 7.1.

7.1 Comparison of different dijet selections

The obtained resolution for three different $|\eta|$ regions, including the reference region, with respect to $p_\mathrm{T,avg}$ and for three $p_\mathrm{T,avg}$ regions in η dependence is shown in Figure 7.2. Additional plots displaying the pseudorapidity regions within $0 < |\eta_\mathrm{probe}| < 4.5$ can be found in Appendix D. The fits used to obtain the JER for the reference regions of each sample are included in Appendix C.

Figures 7.2(a), 7.2(c) and 7.2(e) show the JER in $p_\mathrm{T,avg}$ dependence for the reference region corresponding to $0.2 < |\eta| < 0.7$ and the probe regions $1.3 < |\eta_\mathrm{probe}| < 1.8$ and $1.8 < |\eta_\mathrm{probe}| < 2.5$. The selections tight, nominal and loose are displayed as purple triangles, blue squares and green circles, respectively. The horizontal bars correspond to the $p_\mathrm{T,avg}$ range each data point represents and the vertical bars show the statistical errors obtained from the fits and gaussian error propagation in the calculation.

In general, the plots show the expected behavior of the JER decreasing towards higher transverse momenta, similar to those in Figure 7.1.

Most striking in the results of this thesis, however, is the significant drop of the JER shown by the nominal and loose selection in the first $p_\mathrm{T,avg}$ bin corresponding to $30\,\mathrm{GeV} < p_\mathrm{T,avg} < 40\,\mathrm{GeV}$. This region is particularly sensitive to contributions from soft radiation as the $p_\mathrm{T,3}$ cut, which is supposed to suppress those, is set to $20\,\mathrm{GeV}$, $25\,\mathrm{GeV}$ and $30\,\mathrm{GeV}$ for tight, nominal and loose, respectively. Therefore, soft radiation of the same order of magnitude as jet 1 and 2 is allowed in this region. It would even be possible to contaminate the selection with events where one of the two chosen jets does not originate from the dijet event itself but from an underlying event. To prevent this the $\Delta\phi_{12}$ cut is applied additionally which is set to 2.9, 2.7 and 2.5 for the tight, nominal and loose selection, respectively. The impact of this cut is mainly visible in those low momentum regions where the $p_\mathrm{T,3}$ cut is less restrictive. As can be seen in the JER curves displayed, the resolution of the tight selection does not show this drop which strengthens the presumption that the first $p_\mathrm{T,avg}$ bin is compromised by soft radiation. This allows to explain the deviation from the expected behavior for the nominal and loose selection.
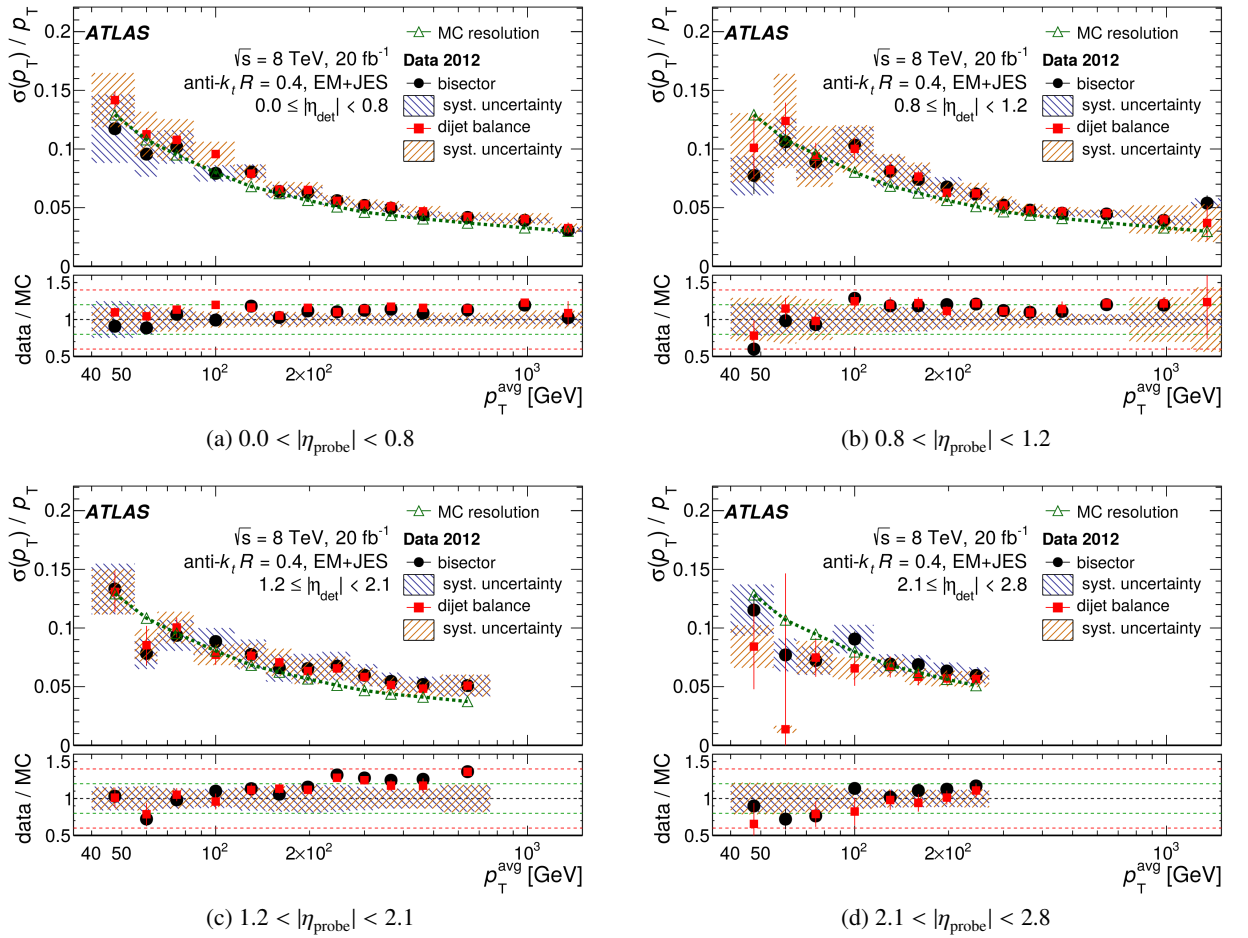
Figure 7.1: Shown are the results of the ATLAS collaboration for data recorded in 2012 at $\sqrt{s} = 8\,\text{TeV}$ published in 2019 [25]. The JER was determined with the bisector method and the dijet balance method which are displayed as black circles and red squares, respectively.

Unfortunately, as can be observed in Figure 7.1 no $p_{\text{T,avg}}$ range lower than $50\,\text{GeV}$ has been investigated in the earlier analysis preventing a potentially interesting comparison of this region.

Hence, the results for the lowest $p_{\text{T,avg}}$ region are considered less relevant when evaluating the performance of the bisector method with the modified fitting procedure which is the subject of this thesis.

In Figures 7.3(b), 7.3(d) and 7.3(e) the JER is displayed in $|\eta_{\text{probe}}|$ dependence for three $p_{\text{T,avg}}$ bins namely $55\,\text{GeV} < p_{\text{T,avg}} < 80\,\text{GeV}$, $150\,\text{GeV} < p_{\text{T,avg}} < 200\,\text{GeV}$ and $550\,\text{GeV} < p_{\text{T,avg}} < 800\,\text{GeV}$ representing a low, medium and high $p_{\text{T,avg}}$ range, respectively. It can be observed that the JER of the loose selection tends to fluctuate stronger than the resolution obtained from the tight and nominal selection with rising tendency towards lower $p_{\text{T,avg}}$. This is anticipated due to the stronger impact of soft radiation as previously discussed in detail.

Generally, the resolution is expected to change with η as the detector itself is not homogeneous but is composed of divers components. The JER increases towards higher pseudorapidity regions, in accordance with the anticipated behavior, as they correspond to outer parts of the detector which is designed to be most precise closest to the collision point.

In conclusion, the different selections show deviations in the expected areas but otherwise good

agreement within statistical uncertainties confirming that the cuts chosen for the nominal selection do not bias the results, at least for $p_{\mathrm{T,avg}} \gtrsim 80\,\mathrm{GeV}$.

7.2 Comparison of data and Monte Carlo

In this section, the JER obtained from data, MC Pythia8 and MC Sherpa (with the nominal dijet selection applied on all samples) is compared and discussed.

The results are displayed for three different $|\eta|$ and $p_{\mathrm{T,avg}}$ regions in Figure 7.3 in the same way as the results for the dijet selection comparison. The plots for the remaining pseudorapidity regions can be found in Appendix D as well.

In Figures 7.3(a), 7.3(c) and 7.3(e) where the p_{T} dependence is displayed, again, the drop of the JER can be observed, combined with an increasing discrepancy between the samples towards low $p_{\mathrm{T,avg}}$. As discussed in detail in the previous section this drop can be retraced to the rising impact of soft radiation, thus, is considered not to be a consequence of the determination method. The deviation of data and Monte Carlo towards low $p_{\mathrm{T,avg}}$ is not surprising as the comparison of the $p_{\mathrm{T,avg}}$ distribution showed the same tendency.

Otherwise, the samples show very good agreement in the reference region which is important as the calculation for the probe regions heavily depends on those results.

The JER obtained from the MC Pythia8 sample displayed as blue squares shows a smooth curve whereas the resolution for data and MC Sherpa show increasing fluctuations for outer pseudorapidity regions. Since the MC Pythia8 sample has better statistics by a factor of ~ 10 this was anticipated.

Concerning, however, is the increase of the JER observable towards higher $p_{\mathrm{T,avg}}$ in Figure 7.3(e). On closer inspection one notices that even the MC Pythia8 sample shows this behavior, i.e. it cannot be discarded as a fluctuation due to low statistics. In Figure 7.4 the fits used to calculate the JER for MC Pythia8 with $1\,100\,\mathrm{GeV} < p_{\mathrm{T,avg}} < 1\,500\,\mathrm{GeV}$ and $1.8 < |\eta_{\mathrm{probe}}| < 2.5$ are displayed. The p_{α} truth and reco distributions look inconspicuous but the p_{β} truth and reco distributions both show an asymmetric behavior. They decrease significantly slower on the left hand side of the peak compared to the right hand side. In consequence, the chosen symmetric functions are unable to model the distributions properly. Such asymmetric distributions were consistently observed for high $p_{\mathrm{T,avg}}$ regions in combination with high $|\eta_{\mathrm{probe}}|$ regions. Those common factors could indicate that this behavior is related to boosted events which occur more often at higher momenta and usually have one jet located in an outer pseudorapidity region of the detector. Since the β-axis is chosen in direction of jet 1[1], this asymmetry states that the average transverse momentum of jets within the reference region is higher than the average transverse momentum of the probe jets.

No further studies investigating this effect have been done due to the limited time resources of this thesis, therefore, it is not possible to make a reliable statement concerning the origins of this asymmetry. It is merely noticed as potential cause of the increasing resolution towards higher $p_{\mathrm{T,avg}}$ in high $|\eta_{\mathrm{probe}}|$ regions.

Looking at the plots in Figure 7.1 which show the results from the ATLAS collaboration one could boldly assume to see this effect for the last $p_{\mathrm{T,avg}}$ region displayed in Figure 7.1(c) representing $1.2 < |\eta_{\mathrm{probe}}| < 2.1$ but this might also be a statistical fluctuation. In the following pseudorapidity region of $2.1 < |\eta_{\mathrm{probe}}| < 2.8$ displayed in Figure 7.1(d), the last $p_{\mathrm{T,avg}}$ region shown is beneath $300\,\mathrm{GeV}$ where the asymmetric behavior does not yet show.

---

[1] Not in the exact direction as the dijet events are usually not perfectly oriented with $\Delta\phi_{12} = \pi$ but such that the β-component of jet 1 is always positive.
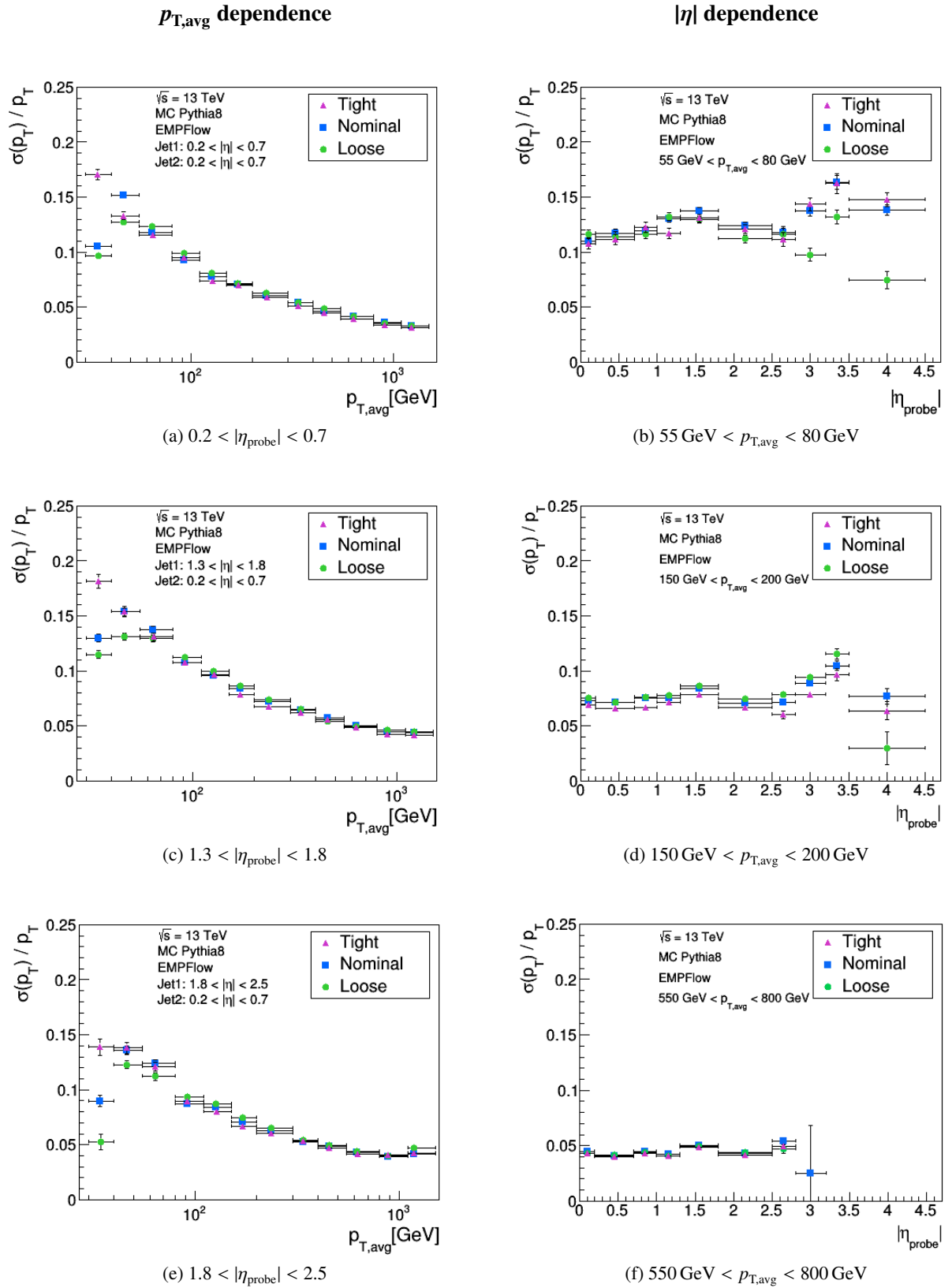
$p_{T,avg}$ dependence   **$|\eta|$ dependence**

(a) $0.2 < |\eta_{probe}| < 0.7$

(b) $55\,\text{GeV} < p_{T,avg} < 80\,\text{GeV}$

(c) $1.3 < |\eta_{probe}| < 1.8$

(d) $150\,\text{GeV} < p_{T,avg} < 200\,\text{GeV}$

(e) $1.8 < |\eta_{probe}| < 2.5$

(f) $550\,\text{GeV} < p_{T,avg} < 800\,\text{GeV}$

Figure 7.2: The JER with respect to $p_{T,avg}$ and $|\eta|$ for tight, nominal and loose dijet selection of the MC Pythia8 sample.

Apart from that, the results meet the expectations showing the anticipated behavior and good agreement within statistical fluctuations for $p_{\mathrm{T,avg}} \gtrsim 80\,\mathrm{GeV}$. Since this was the approximate limit beneath which the impact of soft radiation compromises the dijet selection those results are satisfactory.

$p_{\mathrm{T,avg}}$ dependence

$|\eta|$ dependence

(a) $0.2 < |\eta_{\mathrm{probe}}| < 0.7$

(b) $55\,\mathrm{GeV} < p_{\mathrm{T,avg}} < 80\,\mathrm{GeV}$

(c) $1.3 < |\eta_{\mathrm{probe}}| < 1.8$

(d) $150\,\mathrm{GeV} < p_{\mathrm{T,avg}} < 200\,\mathrm{GeV}$

(e) $1.8 < |\eta_{\mathrm{probe}}| < 2.5$

(f) $550\,\mathrm{GeV} < p_{\mathrm{T,avg}} < 800\,\mathrm{GeV}$
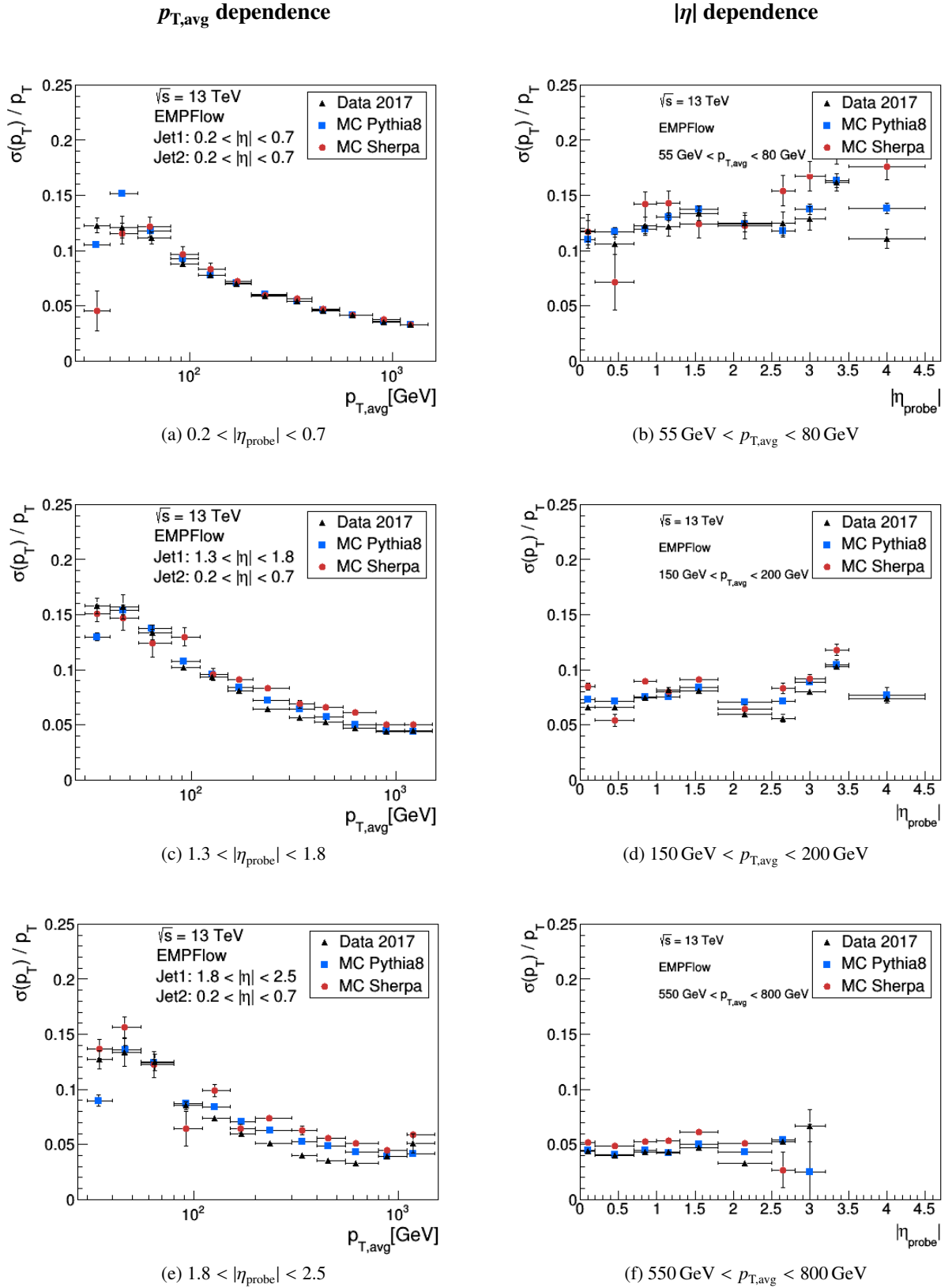
Figure 7.3: The JER with respect to $p_{\mathrm{T,avg}}$ and $|\eta|$ obtained from data, MC Pythia8 and MC Sherpa.
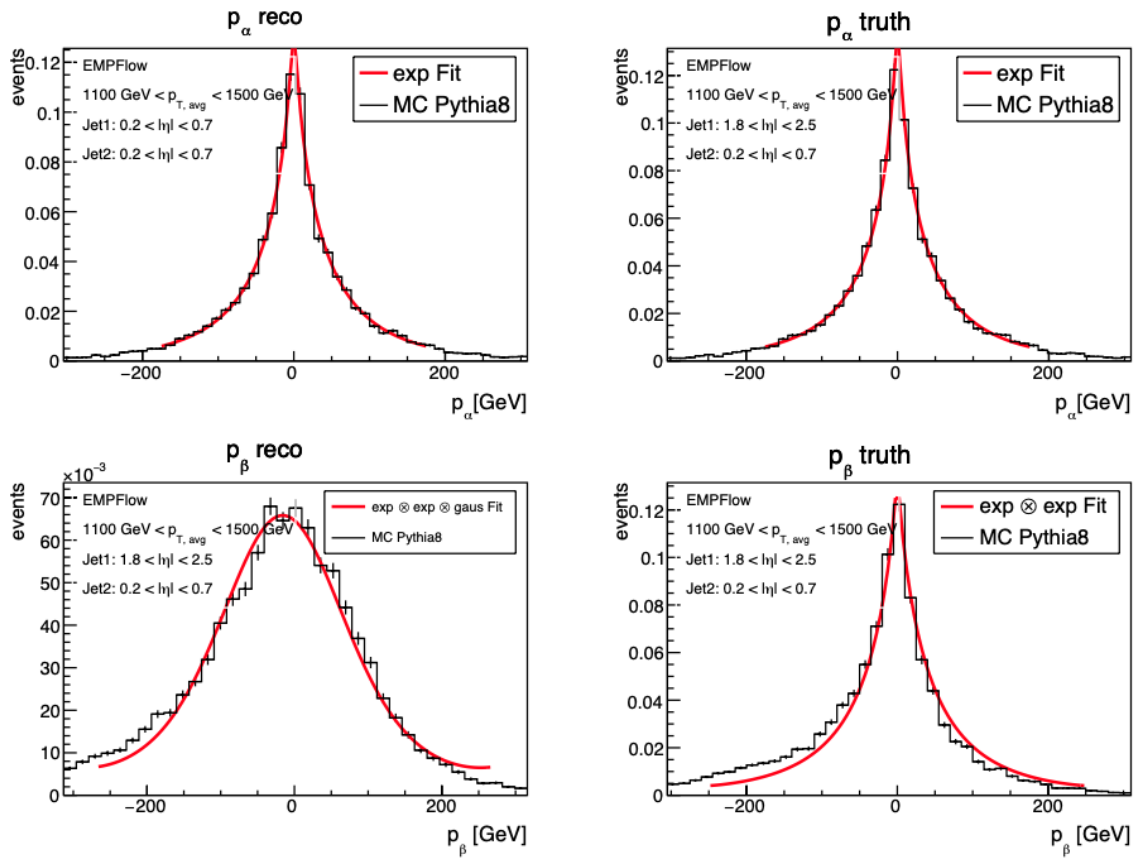
Figure 7.4: MC Pythia8 nominal fits for $1\,100\,\text{GeV} < p_{\text{T,avg}} < 1\,500\,\text{GeV}$ and $1.8 < |\eta_{\text{probe}}| < 2.5$

Conclusion

This chapter summarizes the results of this thesis and gives an outlook to what still needs to be done to improve the stability and precision of the bisector method.

8.1 Summary

In this thesis, the jet energy resolution in proton-proton collisions at $\sqrt{s} = 13\,\text{TeV}$ recorded in 2017 with the ATLAS detector was determined using the bisector method.

To improve the performance of this method, a few alterations were made to the fitting procedure. Namely, the OOC effects which occur along the β-axis are treated as expontially distributed rather than gaussian. As expected, the convolution of two exponential functions proved to be much more suitable to model the p_β^{truth} distribution than the previously used convolution of an exponential function and a Gaussian. Furthermore, the particle level correction via quadratic subtraction is replaced by a second convolution, i.e. the p_β^{reco} distribution is fitted with a convolution of two exponential functions (one of them from the p_α^{reco} fit and the other being the second exponential from the p_β^{truth} fit) with fixed parameters and a Gaussian with floating parameters. Those changes enhanced the quality of the fitting procedure significantly, especially the p_β^{truth} distribution could be modeled more accurately.

The investigation of the different dijet selections confirms a reasonable choice of cuts for the nominal selection. Deviations only occur at low $p_{\text{T,avg}}$ regions which is acceptable as discussed in detail in the previous chapter.

The obtained results for data and Monte Carlo simulated events show good agreement within statistical uncertainties. It is still noticeable that data and MC Sherpa show larger fluctuations which was expected due to their lower statistics but the Sherpa fluctuations were reduced compared to previous attempts.

8.2 Outlook

As indicated during the discussion of the results in the last chapter, there are still some kinks linked to this method of deriving the JER that require further investigation.

The region of transverse momenta beneath approximately $80\,\text{GeV}$ could be studied in more detail with emphasis on contributions from soft radiation. Related to that, it could be useful to get a better understanding of the impact of FSR, again, mainly for the low p_{T} regions.

The more urgent matter, however, are the shown asymmetric distributions for high p_{T} in high $|\eta_{\text{probe}}|$ regions as the bisector method is unable to handle those properly. Since the dijet balance method uses

the assumption $\left\langle p_T^{\text{probe}} \right\rangle = \left\langle p_T^{\text{ref}} \right\rangle = \left\langle p_{\text{T,avg}} \right\rangle$ to obtain Equation 5.5, it would presumably be effected by this issue as well. Therefore, a more detailed study is necessary to precisely determine the JER in those regions addressed.

Bibliography

[1]   M. Thomson, *Modern Particle Physics*, Cambridge University Press, 2013 (cit. on p. 3).

[2]   P. W. Higgs, *Broken Symmetries and the Masses of Gauge Bosons*,
       Phys. Rev. Lett. **13** (16 1964) 508,
       URL: https://link.aps.org/doi/10.1103/PhysRevLett.13.508 (cit. on p. 4).

[3]   The ATLAS collaboration, *Observation of a new particle in the search for the Standard Model
       Higgs boson with the ATLAS detector at the LHC*, Physics Letters B **716** (2012) 1,
       ISSN: 0370-2693, URL: http://dx.doi.org/10.1016/j.physletb.2012.08.020
       (cit. on p. 4).

[4]   G. Zweig, *An SU$_3$ model for strong interaction symmetry and its breaking; Version 1*,
       tech. rep. CERN-TH-401, CERN, 1964, URL: http://cds.cern.ch/record/352337
       (cit. on p. 4).

[5]   The ATLAS collaboration,
       Observation of J/ψp Resonances Consistent with Pentaquark States in $\Lambda_b \to J/\psi K^- p$ Decays,
       Physical Review Letters **115** (2015), ISSN: 1079-7114,
       URL: http://dx.doi.org/10.1103/PhysRevLett.115.072001 (cit. on p. 4).

[6]   The ATLAS collaboration, *Observation of J/ψφ Structures Consistent with Exotic States from
       Amplitude Analysis of $B^+ \to J/\psi\phi K^+$ Decays*, Physical Review Letters **118** (2017),
       ISSN: 1079-7114, URL: http://dx.doi.org/10.1103/PhysRevLett.118.022003
       (cit. on p. 4).

[7]   Wikibooks, *A-level Physics (Advancing Physics)/The Standard Model*,
       URL: https://en.wikibooks.org/wiki/A-
       level_Physics_(Advancing_Physics)/The_Standard_Model (cit. on p. 5).

[8]   CERN, *LHC overview*, URL: http://www.lhc-facts.ch/ (cit. on p. 8).

[9]   Garelli, Nicoletta, *Performance of the ATLAS Detector in Run-2*,
       EPJ Web Conf. **164** (2017) 01021,
       URL: https://doi.org/10.1051/epjconf/201716401021 (cit. on p. 7).

[10]   The ATLAS collaboration, *Computer generated image of the ATLAS detector*,
       URL: https://atlas.cern/discover/detector (cit. on p. 9).

[11]   N. Ilić, "Observation of the Higgs Boson decaying to $WW^* \to \ell\nu\ell\nu$", 2015 (cit. on p. 9).

[12]   The ATLAS collaboration, *ATLAS pixel detector electronics and sensors*,
       Journal of Instrumentation **3** (2008) P07007,
       URL: https://doi.org/10.1088%2F1748-0221%2F3%2F07%2Fp07007 (cit. on p. 9).

[13]   The ATLAS collaboration, *Operation and performance of the ATLAS semiconductor tracker*,
       Journal of Instrumentation **9** (2014) P08009, ISSN: 1748-0221,
       URL: http://dx.doi.org/10.1088/1748-0221/9/08/P08009 (cit. on p. 9).

[14]   V. A. MITSOU, *The ATLAS Transition Radiation Tracker*,
Astroparticle, Particle and Space Physics, Detectors and Medical Physics Applications (2004),
URL: http://dx.doi.org/10.1142/9789812702708_0073 (cit. on p. 10).

[15]   The ATLAS collaboration,
Expected performance of the ATLAS experiment: detector, trigger and physics, CERN, 2009,
URL: http://cds.cern.ch/record/1125884 (cit. on p. 10).

[16]   N. Nikiforou, *Performance of the ATLAS Liquid Argon Calorimeter after three years of LHC
operation and plans for a future upgrade*, 2013, arXiv: 1306.6756 [physics.ins-det]
(cit. on p. 11).

[17]   A. Artamonov et al., *The ATLAS Forward Calorimeter*,
Journal of Instrumentation **3** (2008) P02010,
URL: https://doi.org/10.1088%2F1748-0221%2F3%2F02%2Fp02010 (cit. on p. 11).

[18]   M. Mlynarikova, *Upgrade of the ATLAS hadronic Tile calorimeter for the High luminosity LHC*,
2017, arXiv: 1709.00099 [physics.ins-det] (cit. on p. 11).

[19]   J. Pequenao, "Computer Generated image of the ATLAS calorimeter", 2008,
URL: https://cds.cern.ch/record/1095927 (cit. on p. 11).

[20]   The ATLAS collaboration,
Topological cell clustering in the ATLAS calorimeters and its performance in LHC Run 1,
The European Physical Journal C **77** (2017), ISSN: 1434-6052,
URL: http://dx.doi.org/10.1140/epjc/s10052-017-5004-5 (cit. on pp. 13, 14).

[21]   The ATLAS collaboration,
Jet reconstruction and performance using particle flow with the ATLAS Detector,
The European Physical Journal C **77** (2017), ISSN: 1434-6052,
URL: http://dx.doi.org/10.1140/epjc/s10052-017-5031-2 (cit. on pp. 13–15).

[22]   R. Atkin, *Review of jet reconstruction algorithms*,
Journal of Physics: Conference Series **645** (2015) 012008,
URL: https://doi.org/10.1088%2F1742-6596%2F645%2F1%2F012008 (cit. on pp. 14, 19).

[23]   M. Cacciari, G. P. Salam and G. Soyez, *The anti-ktjet clustering algorithm*,
Journal of High Energy Physics **2008** (2008) 063, ISSN: 1029-8479,
URL: http://dx.doi.org/10.1088/1126-6708/2008/04/063 (cit. on p. 16).

[24]   C. Ay et al., *Monte Carlo generators in ATLAS software*,
Journal of Physics: Conference Series **219** (2010) 032001,
URL: https://doi.org/10.1088%2F1742-6596%2F219%2F3%2F032001 (cit. on p. 16).

[25]   The ATLAS collaboration, *Determination of jet calibration and energy resolution in
proton-proton collisions at $\sqrt{s} = 8$ TeV using the ATLAS detector*, tech. rep. arXiv:1910.04482,
CERN, 2019, URL: https://cds.cern.ch/record/2693121 (cit. on pp. 17, 20, 34).

[26]   *A study of the Pythia 8 description of ATLAS minimum bias measurements with the
Donnachie-Landshoff diffractive model*, tech. rep. ATL-PHYS-PUB-2016-017, CERN, 2016,
URL: https://cds.cern.ch/record/2206965 (cit. on p. 17).

[27]   E. Bothmann et al., *Event generation with Sherpa 2.2*, SciPost Physics **7** (2019), ISSN: 2542-4653,
URL: http://dx.doi.org/10.21468/SciPostPhys.7.3.034 (cit. on p. 17).

[28]   B. P. Jaeger et al., *In situ measurements of the ATLAS jet energy resolution using 13 TeV pp data*,
(2019), URL: http://cds.cern.ch/record/2661735 (cit. on p. 19).

[29] *Determination of the jet energy scale and resolution at ATLAS using Z/γ–jet events in data at* $\sqrt{s}$ = 8 *TeV*, tech. rep. ATLAS-CONF-2015-057, CERN, 2015,
URL: https://cds.cern.ch/record/2059846 (cit. on p. 19).

[30] The ATLAS collaboration, *Jet energy resolution in 2017 data and simulation*,
accessed 05.02.2020,
URL: https://atlas.web.cern.ch/Atlas/GROUPS/PHYSICS/PLOTS/JETM-2018-005/
(cit. on p. 21).

[31] The ATLAS collaboration, *Jet energy resolution in proton-proton collisions at* $\sqrt{s}$ = 7 *TeV recorded in 2010 with the ATLAS detector*, The European Physical Journal C **73** (2013),
ISSN: 1434-6052, URL: http://dx.doi.org/10.1140/epjc/s10052-013-2306-0
(cit. on p. 21).

[32] T. Holm, *Determining the jet energy resolution of the ATLAS detector using the bisector method*,
MA thesis: Rheinische Friedrich-Wilhelms-Universitaet Bonn, 2018 (cit. on pp. 22, 27).

[33] *Luminosity determination in pp collisions at* $\sqrt{s}$ = 13 *TeV using the ATLAS detector at the LHC*,
tech. rep. ATLAS-CONF-2019-021, CERN, 2019,
URL: http://cds.cern.ch/record/2677054 (cit. on p. 25).

Event selection

More detailed information on the used data and MC samples (shown in Table A.1) is given in this part of the appendix. The event selection is presented in Table A.2, more information about the applied cuts is listed in Table 6.1.

Data	
good run list	data17_13TeV.periodAllYear_DetStatus-v97-pro21-17_Unknown_PHYS_StandardGRL_All_Good_25ns_JetHLT_Normal2017.xml
productionTag	p3601
Monte Carlo	
campaign	MC16d
productionTag	p3600

Table A.1: Information about the samples used in this thesis.

MC cleaning	$\frac{p_{\mathrm{T,avg}}}{p_{T,leading}} < 2.0$
leading jet p_{T}	$p_{\mathrm{T, leading}} \geq 15\,\mathrm{GeV}$
distance of primary vertices truth and reco	$Z(\mathrm{PV})_0 - Z(\mathrm{PV})_{0,\,\mathrm{truth}} < 0.1$
jet vertex trigger (JVT)	0.2

Table A.2: Information about the event selection used in this thesis.

Data MC Sherpa comparisons

Here are the MC data comparisons for the Sherpa sample. Since they show less agreement this thesis is mainly focused on the Pythia8 sample.

(a)   (b)
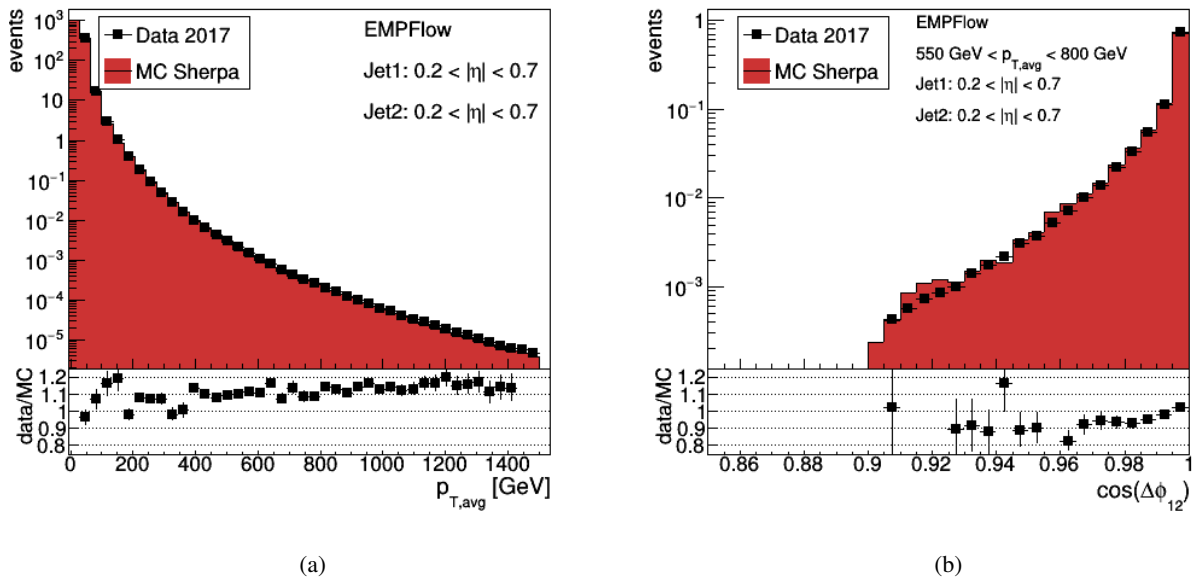
Figure B.1: comparison of data and MC Sherpa is shown for $p_{\mathrm{T,avg}}$ (a) and $\cos(\Delta\phi_{12})$ (b).

Additional Fits

Figure C.1 shows an example of the full performance of the advanced convolution method for an outer pseudorapidity region of $2.8 < |\eta_{\text{probe}}\text{probe}| < 3.2$. Figures C.2 to C.11 the fits used to obtain the JER in
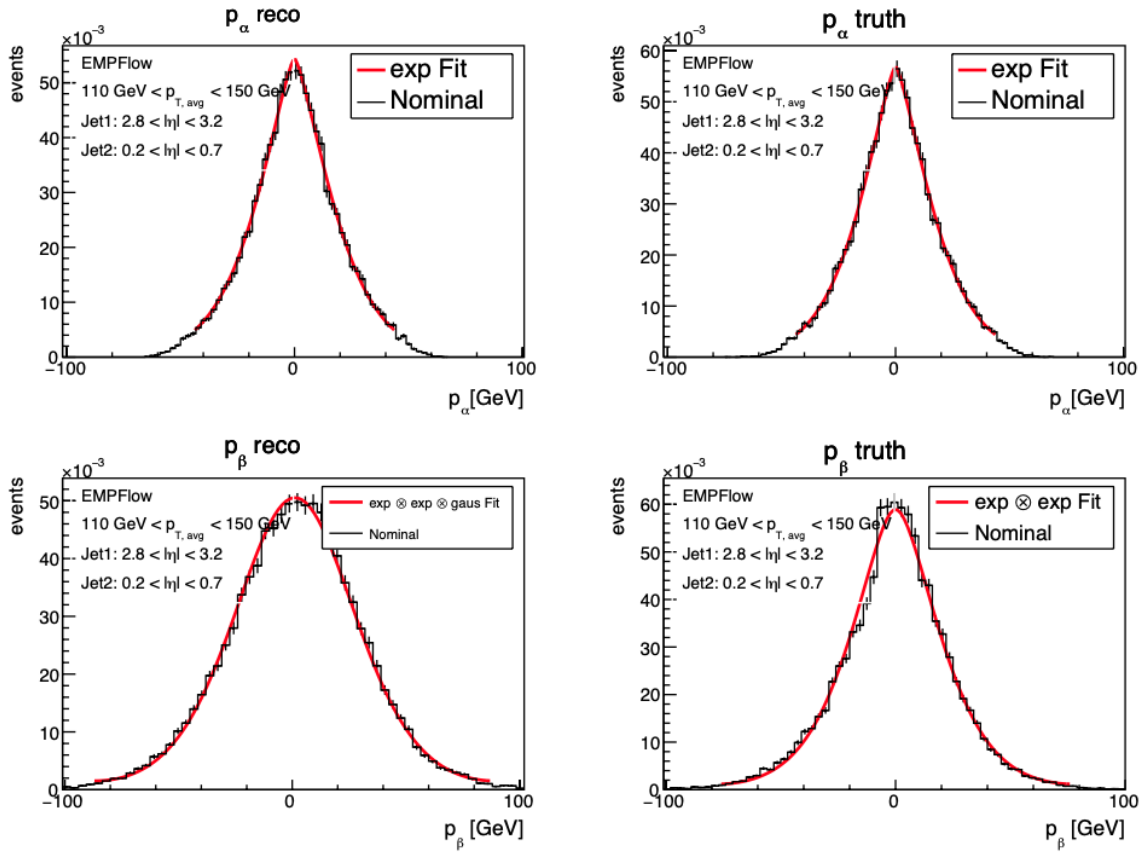
Figure C.1: One full performance of the advanced convolution method is shown for $110\,\text{GeV} < p_{\text{T,avg}} < 150\,\text{GeV}$ and $2.8 < |\eta_{\text{probe}}| < 3.2$. The distributions are simulated with the MC generator Pythia8.

the reference region for data, MC Sherpa and MC Pythia8 (tight, nominal and loose). The columns show the p_α^{reco}, p_α^{truth}, p_β^{reco} and p_β^{truth} distributions from left to right.
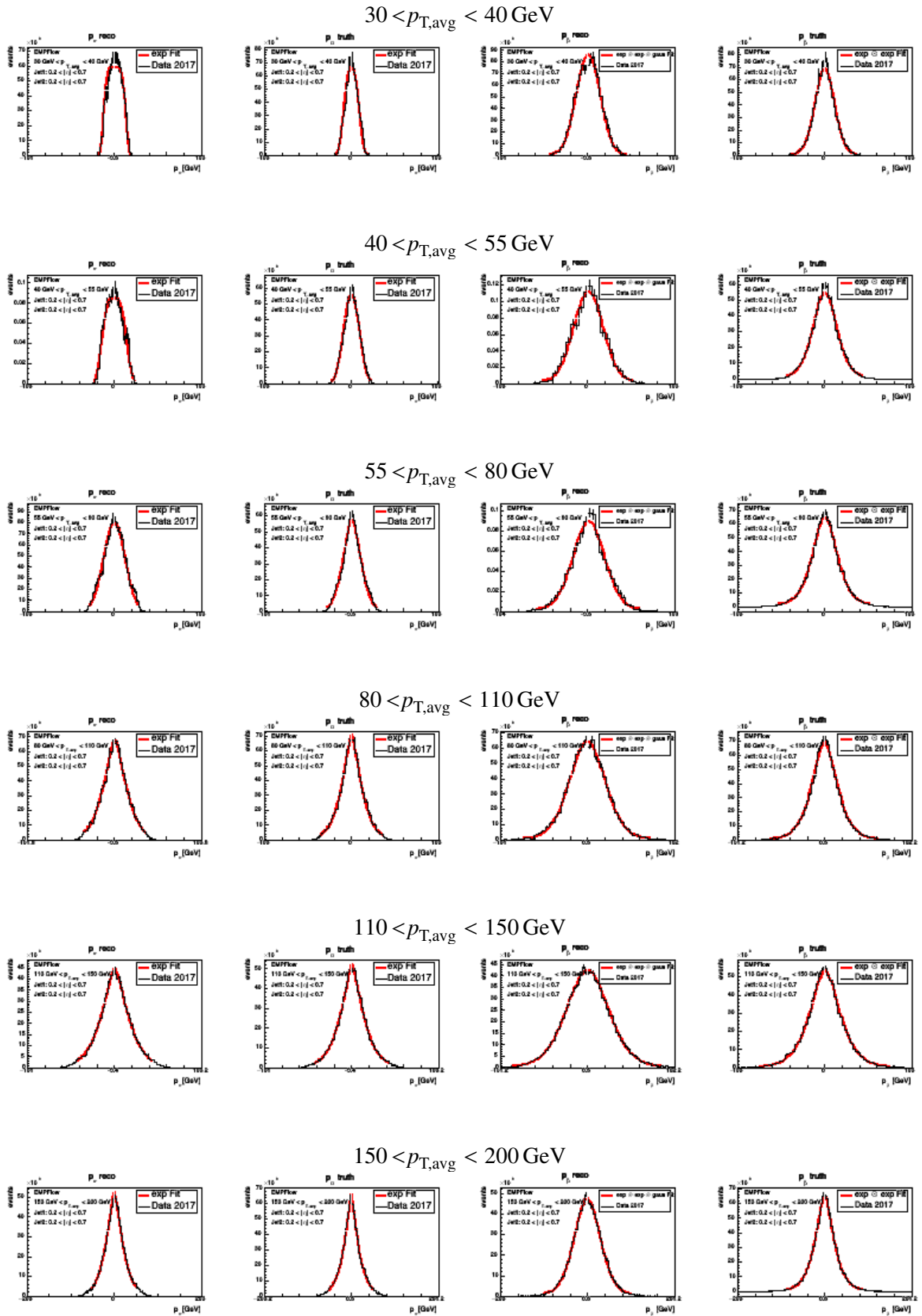
Figure C.2: Data 2017 fits I

$200 < p_{\mathrm{T,avg}} < 300\,\mathrm{GeV}$

$300 < p_{\mathrm{T,avg}} < 400\,\mathrm{GeV}$

$400 < p_{\mathrm{T,avg}} < 550\,\mathrm{GeV}$

$550 < p_{\mathrm{T,avg}} < 800\,\mathrm{GeV}$

$800 < p_{\mathrm{T,avg}} < 1\,100\,\mathrm{GeV}$

$1\,100 < p_{\mathrm{T,avg}} < 1\,500\,\mathrm{GeV}$
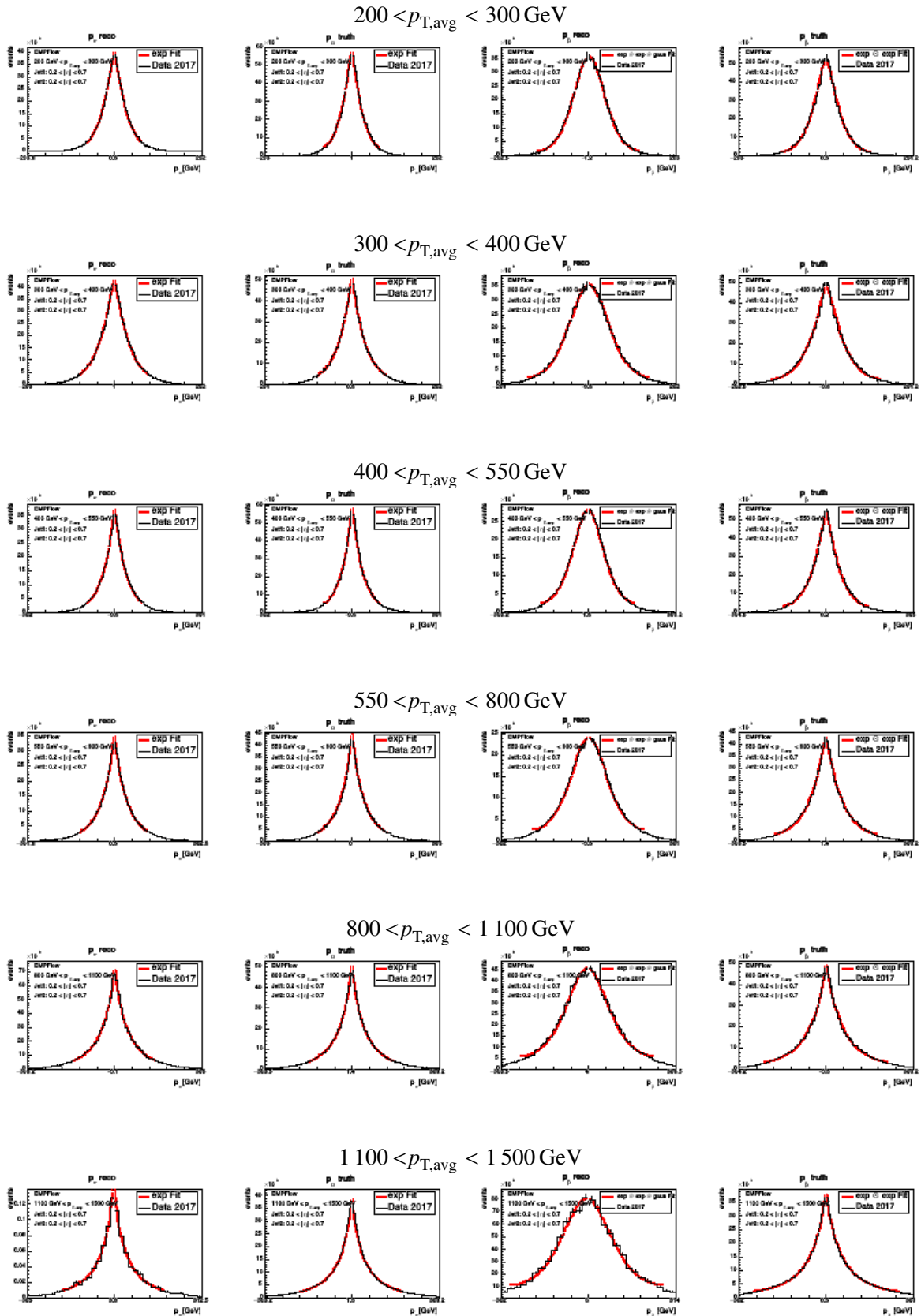
Figure C.3: Data 2017 fits II

$30 < p_{\text{T,avg}} < 40\,\text{GeV}$

$40 < p_{\text{T,avg}} < 55\,\text{GeV}$

$55 < p_{\text{T,avg}} < 80\,\text{GeV}$

$80 < p_{\text{T,avg}} < 110\,\text{GeV}$

$110 < p_{\text{T,avg}} < 150\,\text{GeV}$

$150 < p_{\text{T,avg}} < 200\,\text{GeV}$
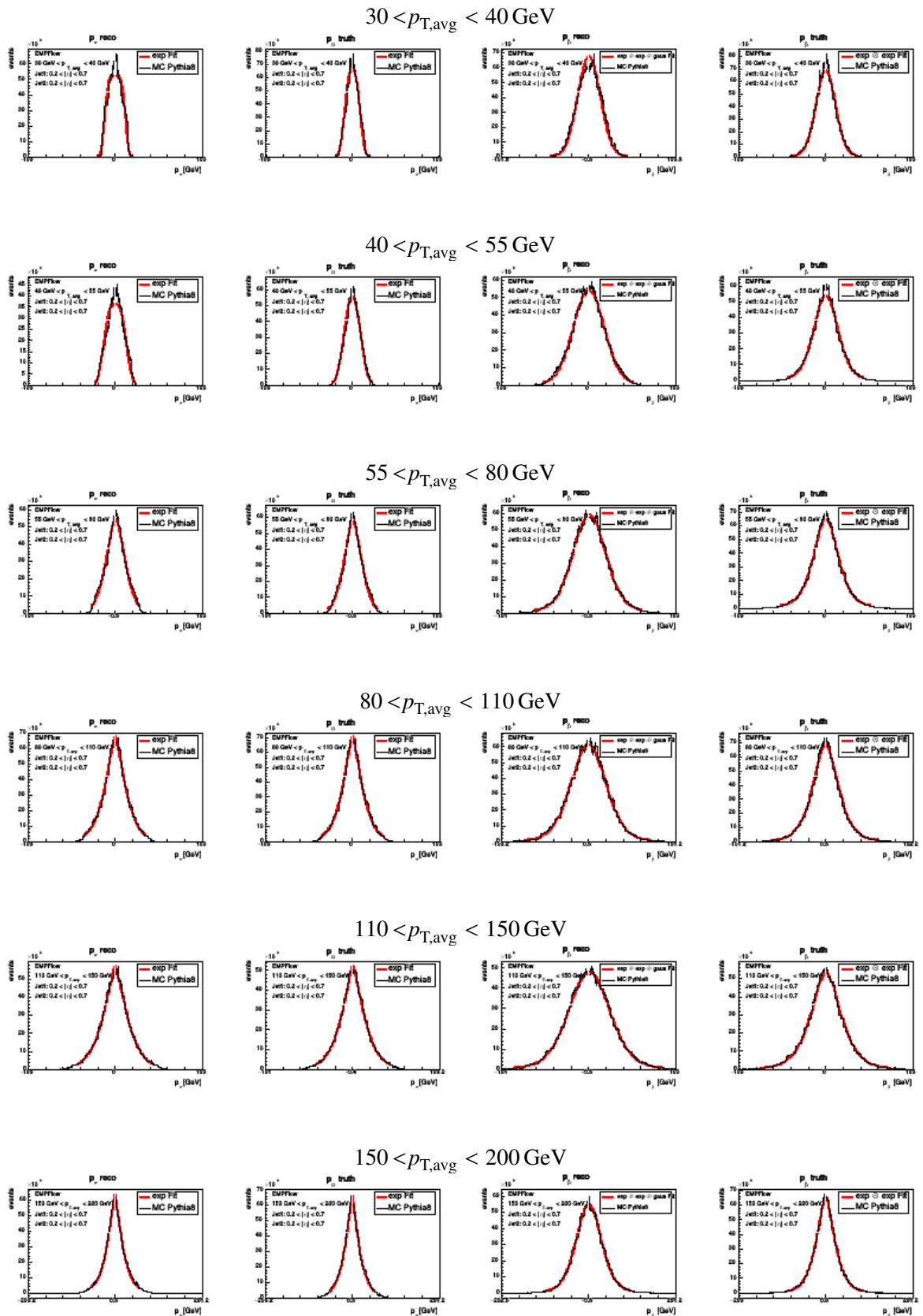
Figure C.4: MC Pythia8 nominal dijet selection fits I
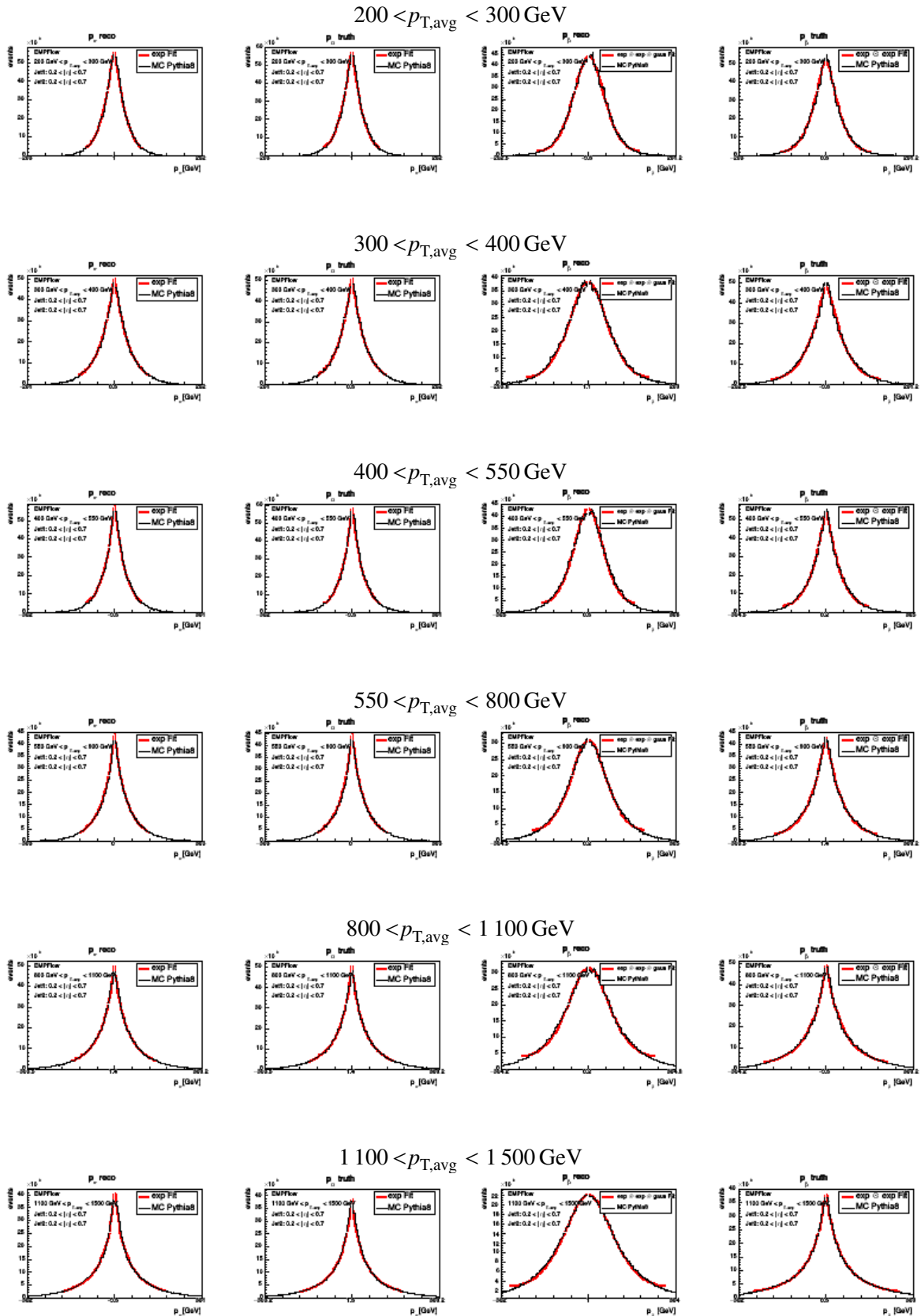
Figure C.5: MC Pythia8 nominal dijet selection fits II
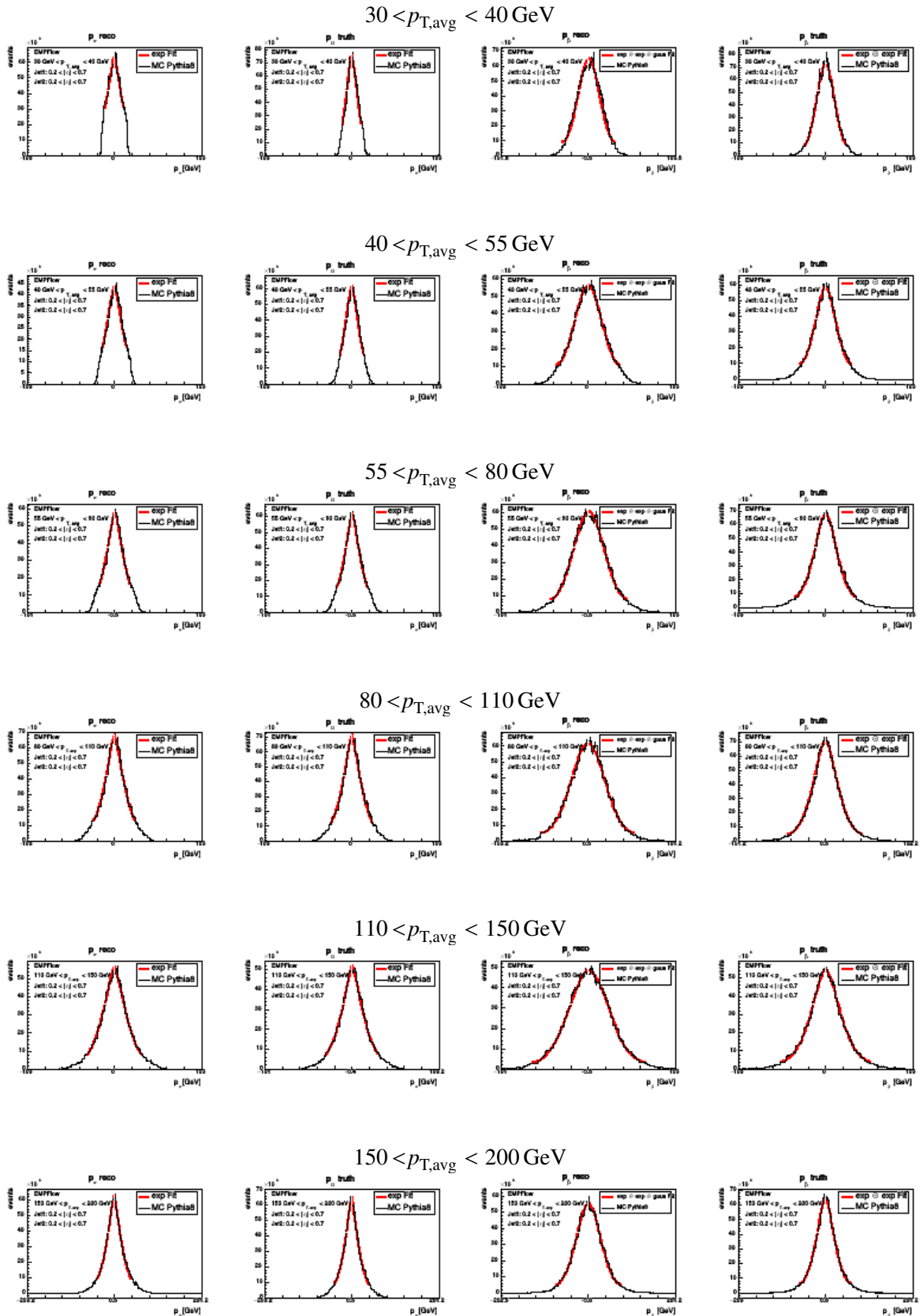
Figure C.6: MC Pythia8 tight dijet selection fits I
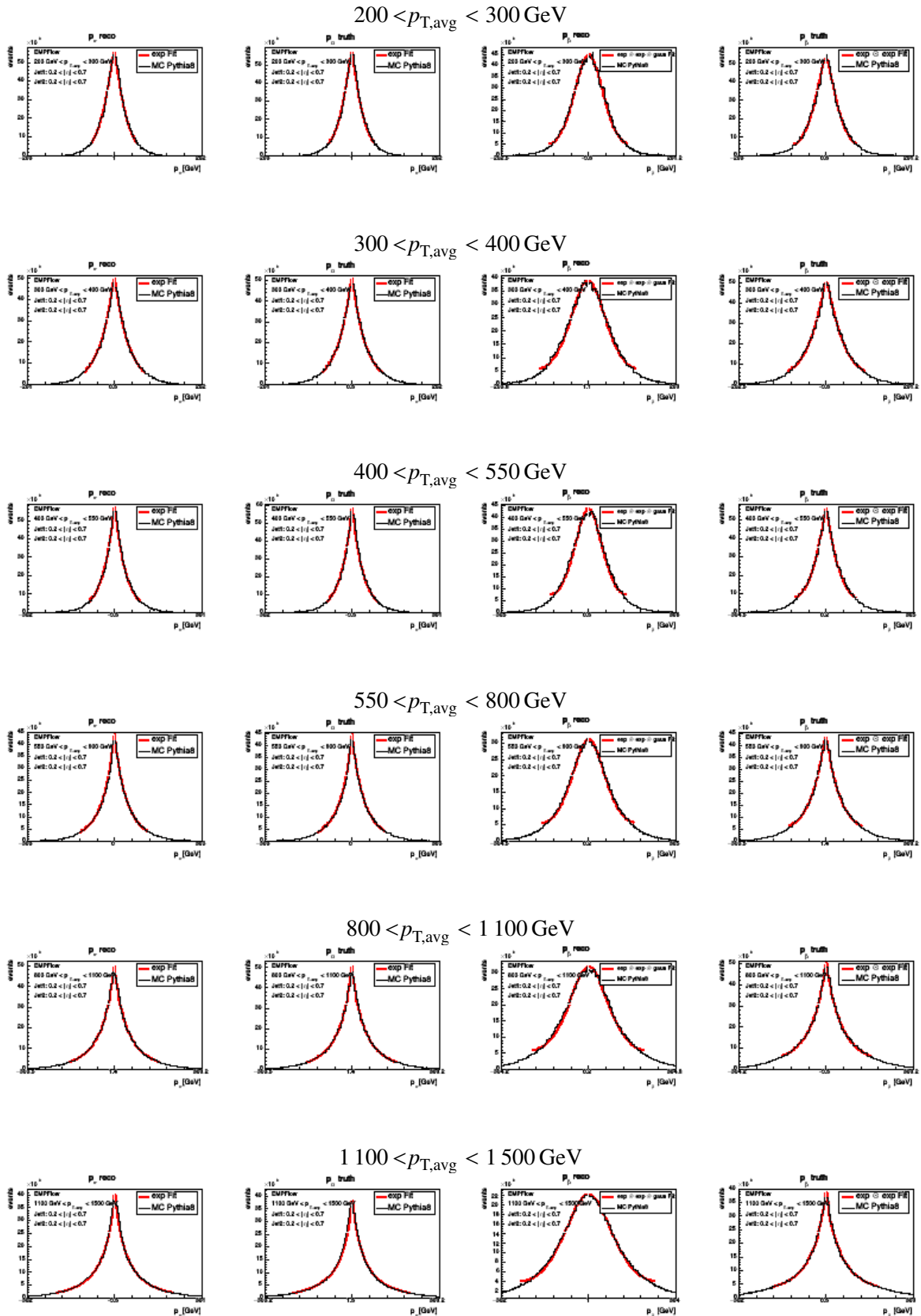
Figure C.7: MC Pythia8 tight dijet selection fits II

$30 < p_{\text{T,avg}} < 40\,\text{GeV}$

$40 < p_{\text{T,avg}} < 55\,\text{GeV}$

$55 < p_{\text{T,avg}} < 80\,\text{GeV}$

$80 < p_{\text{T,avg}} < 110\,\text{GeV}$

$110 < p_{\text{T,avg}} < 150\,\text{GeV}$

$150 < p_{\text{T,avg}} < 200\,\text{GeV}$
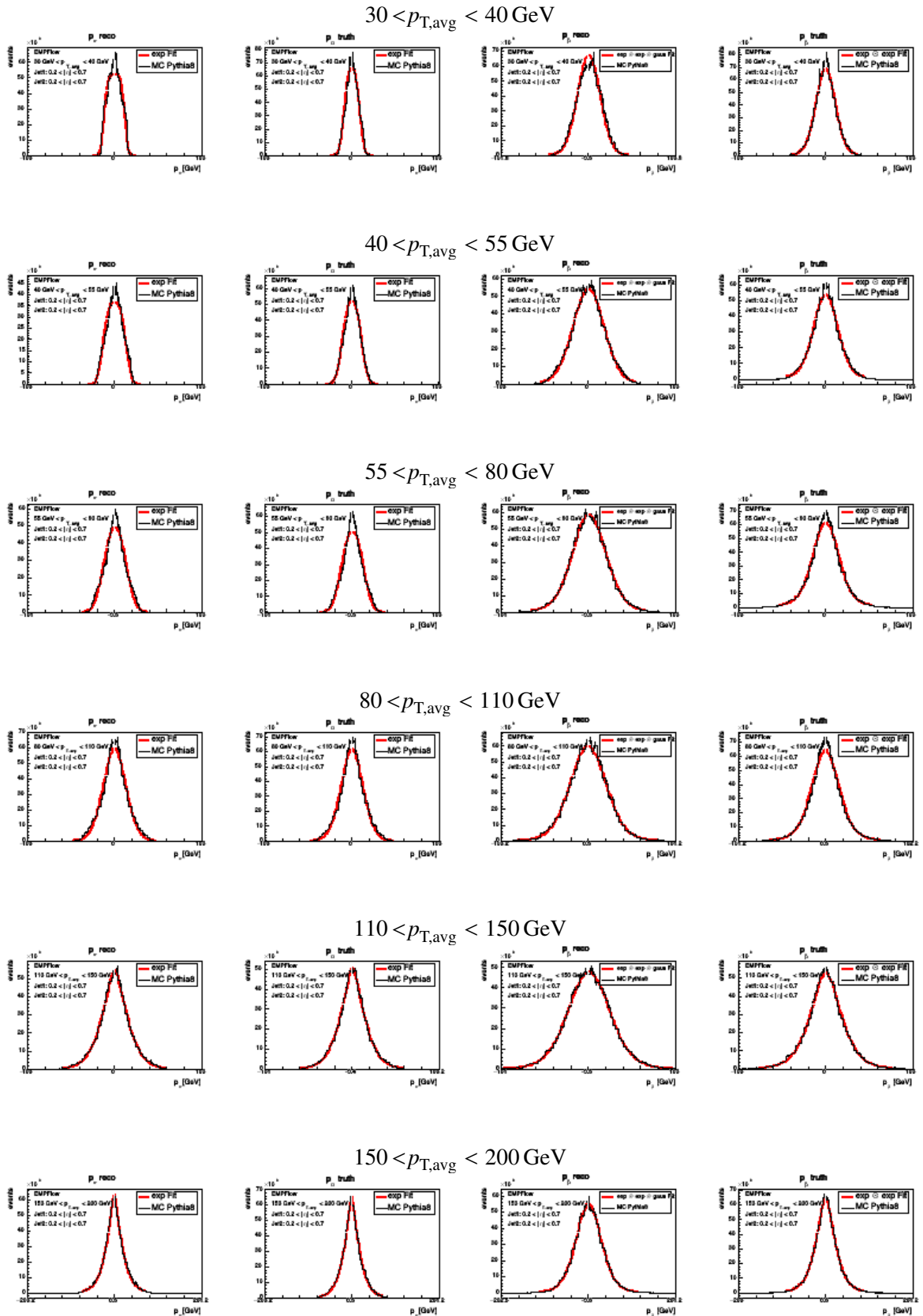
Figure C.8: MC Pythia8 loose dijet selection fits I
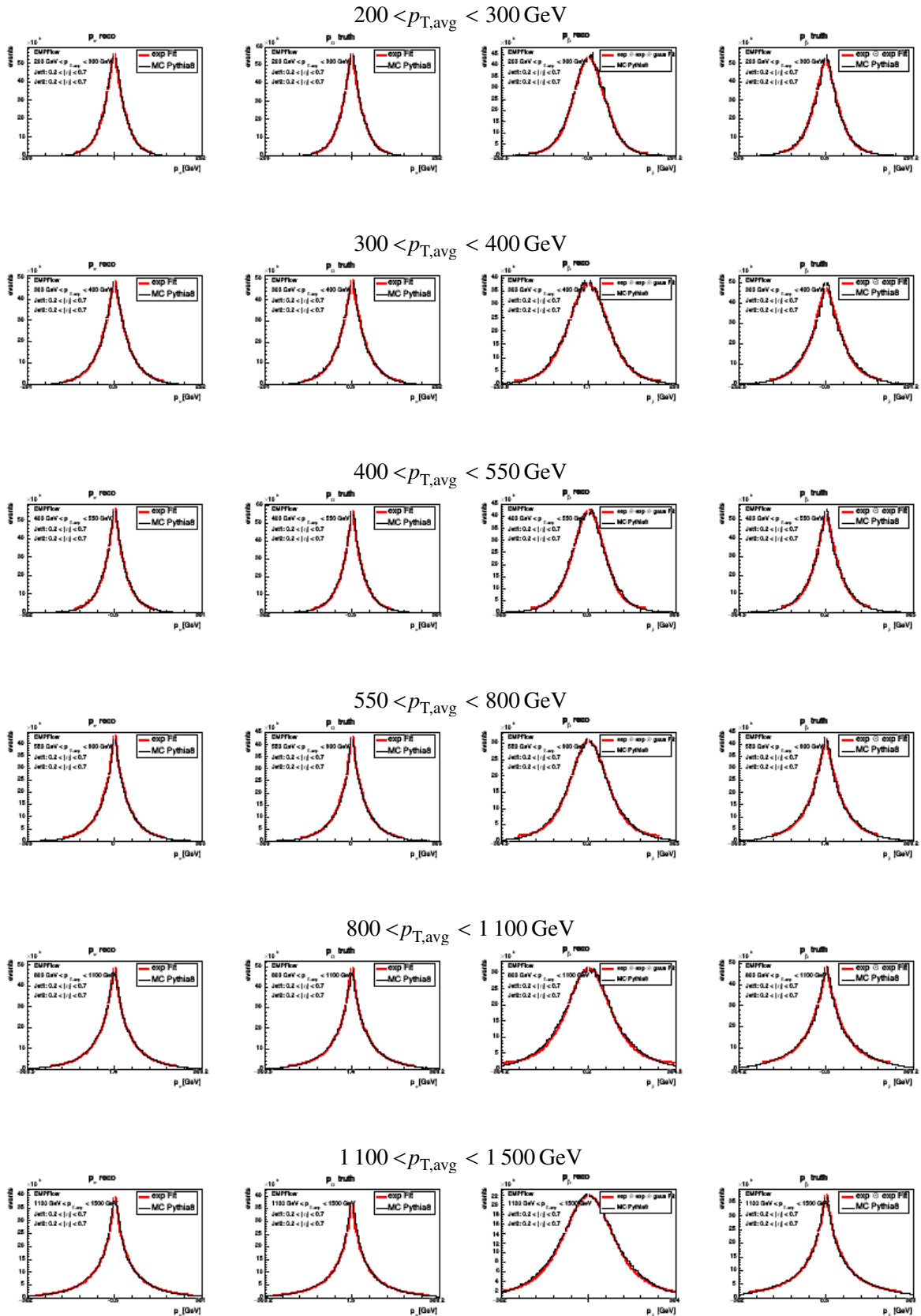
Figure C.9: MC Pythia8 loose dijet selection fits II

$30 < p_{T,avg} < 40\,\text{GeV}$

$40 < p_{T,avg} < 55\,\text{GeV}$

$55 < p_{T,avg} < 80\,\text{GeV}$

$80 < p_{T,avg} < 110\,\text{GeV}$

$110 < p_{T,avg} < 150\,\text{GeV}$

$150 < p_{T,avg} < 200\,\text{GeV}$
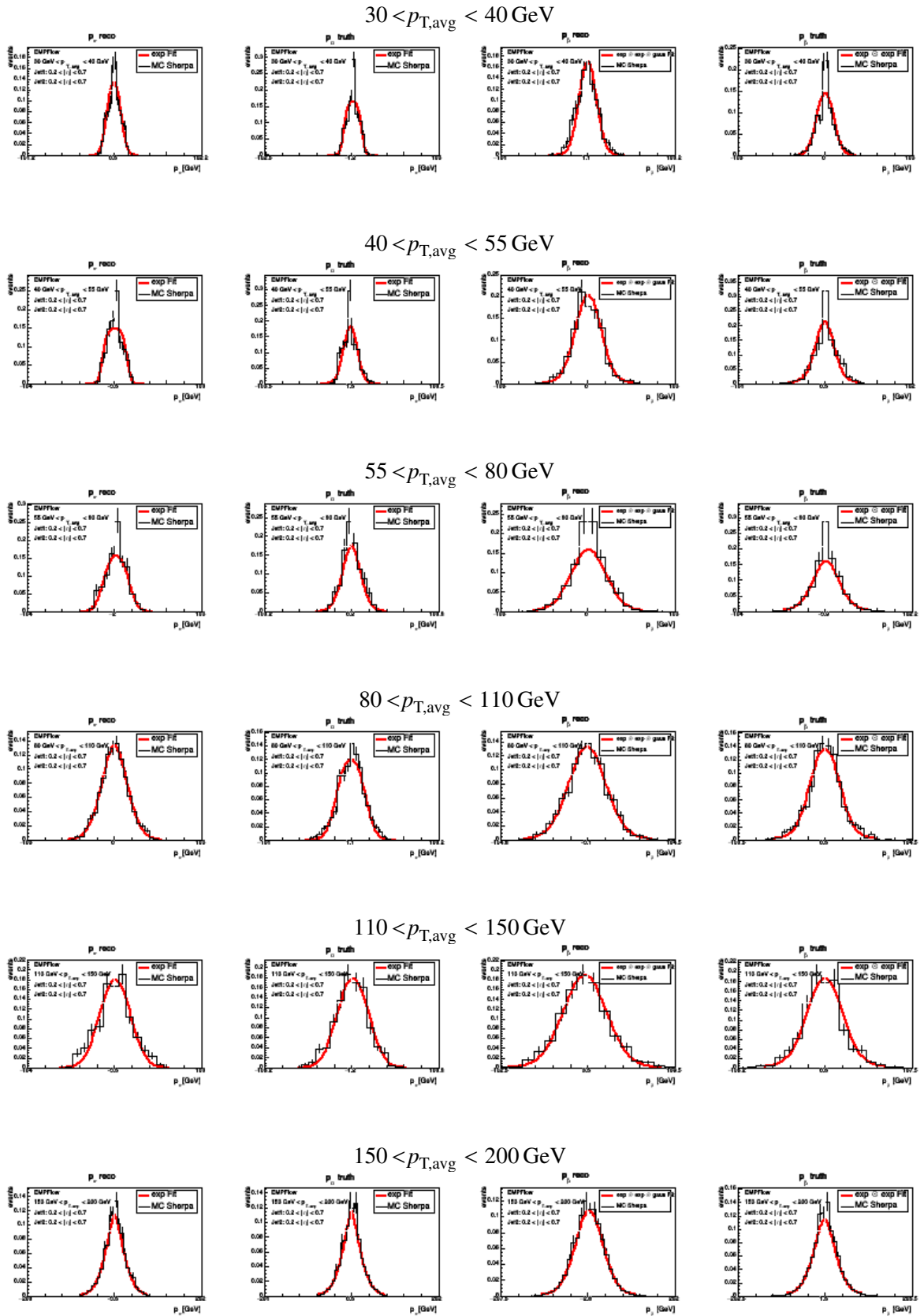
Figure C.10: MC Sherpa fits I

$200 < p_{\text{T,avg}} < 300\,\text{GeV}$

$300 < p_{\text{T,avg}} < 400\,\text{GeV}$

$400 < p_{\text{T,avg}} < 550\,\text{GeV}$

$550 < p_{\text{T,avg}} < 800\,\text{GeV}$

$800 < p_{\text{T,avg}} < 1\,100\,\text{GeV}$

$1\,100 < p_{\text{T,avg}} < 1\,500\,\text{GeV}$
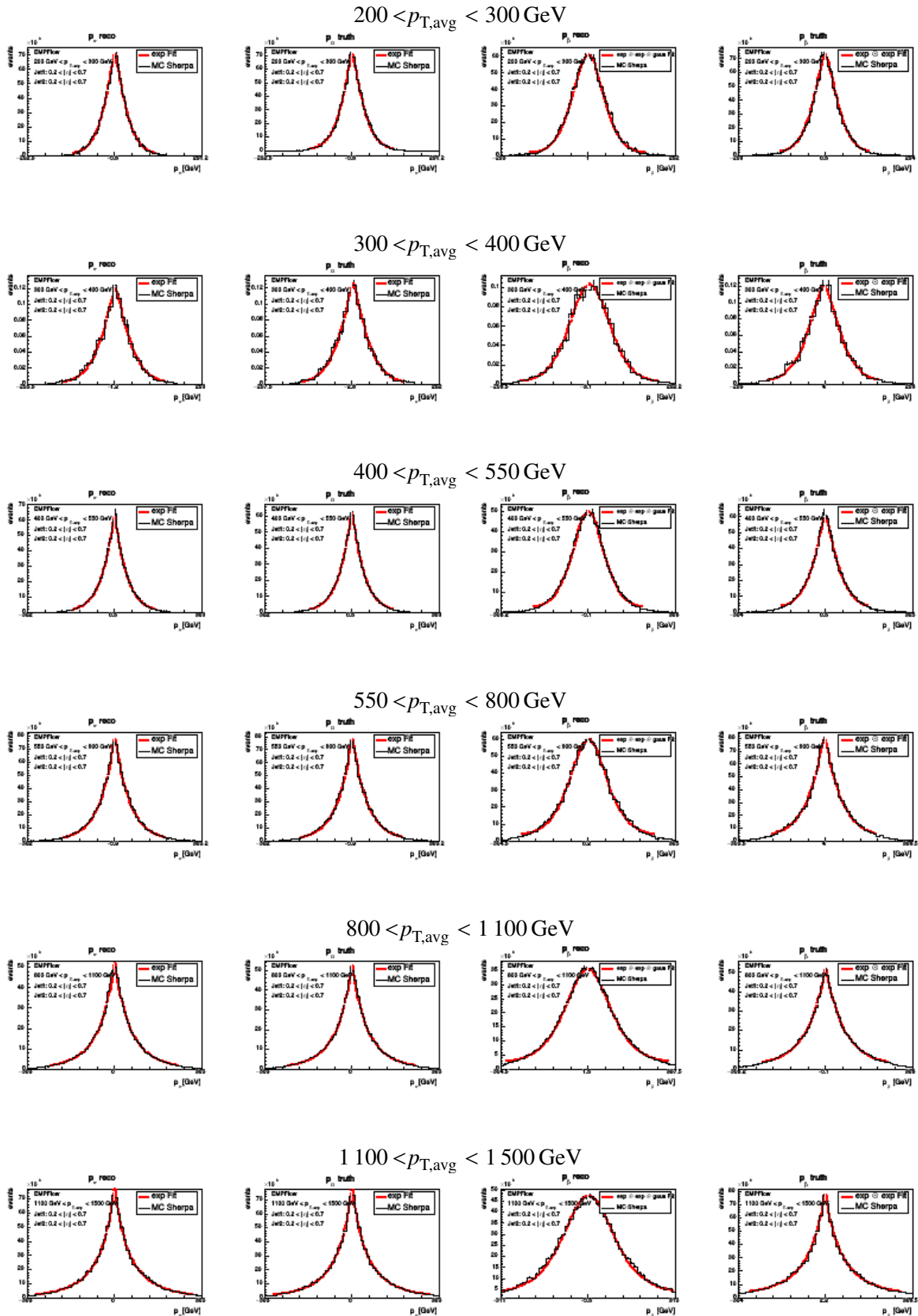
Figure C.11: MC Sherpa fits II

Additional JER plots

In this part the JER plots for all pseudorapidity regions are shown.

D.1 Data/MC
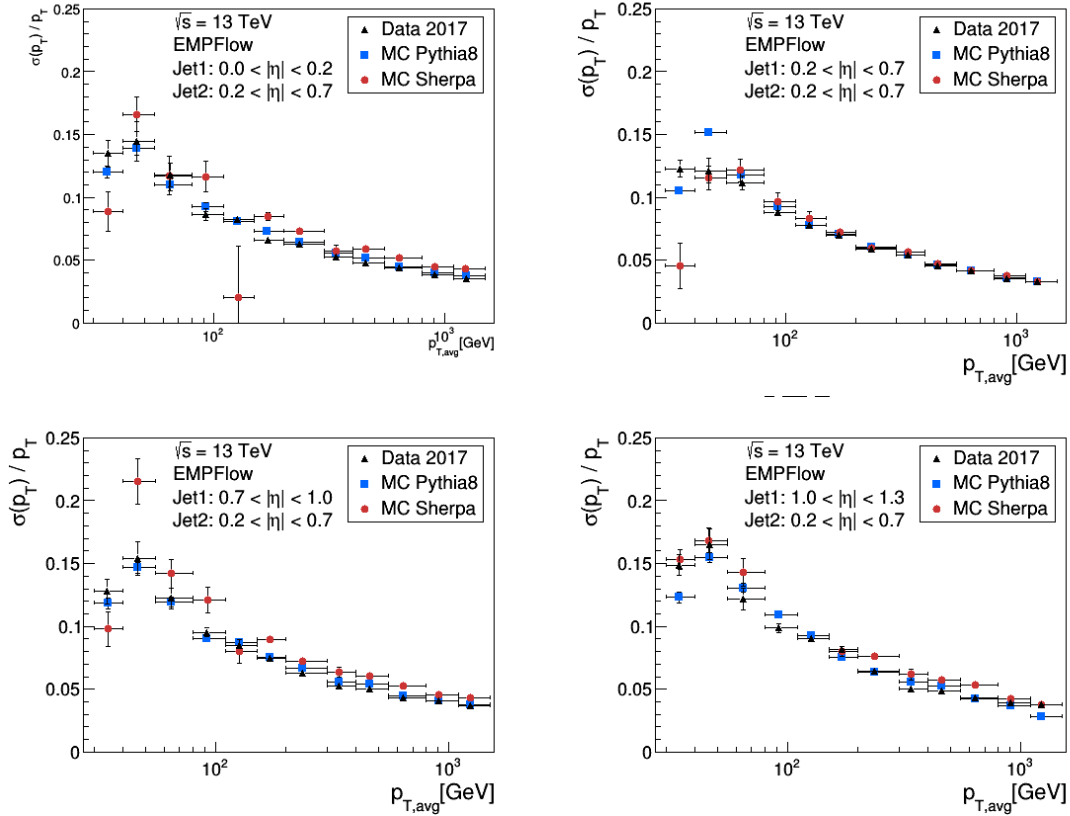
Figure D.1: Additional JER plots of data, MC Pythia8 and MC Sherpa are shown.
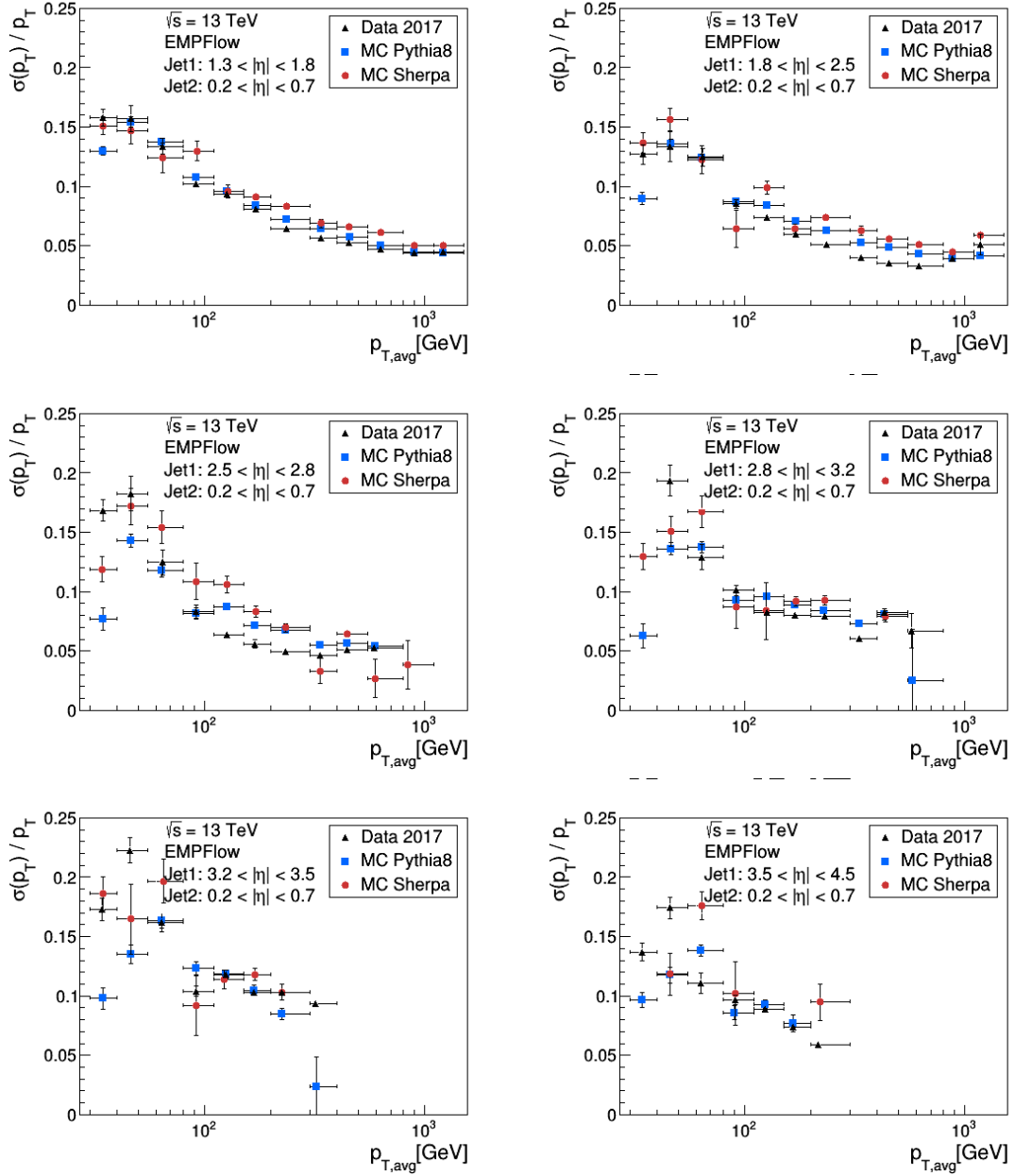
Figure D.2: Additional JER plots of data, MC Pythia8 and MC Sherpa are shown.

D.2 MC Pythia8 dijet selection
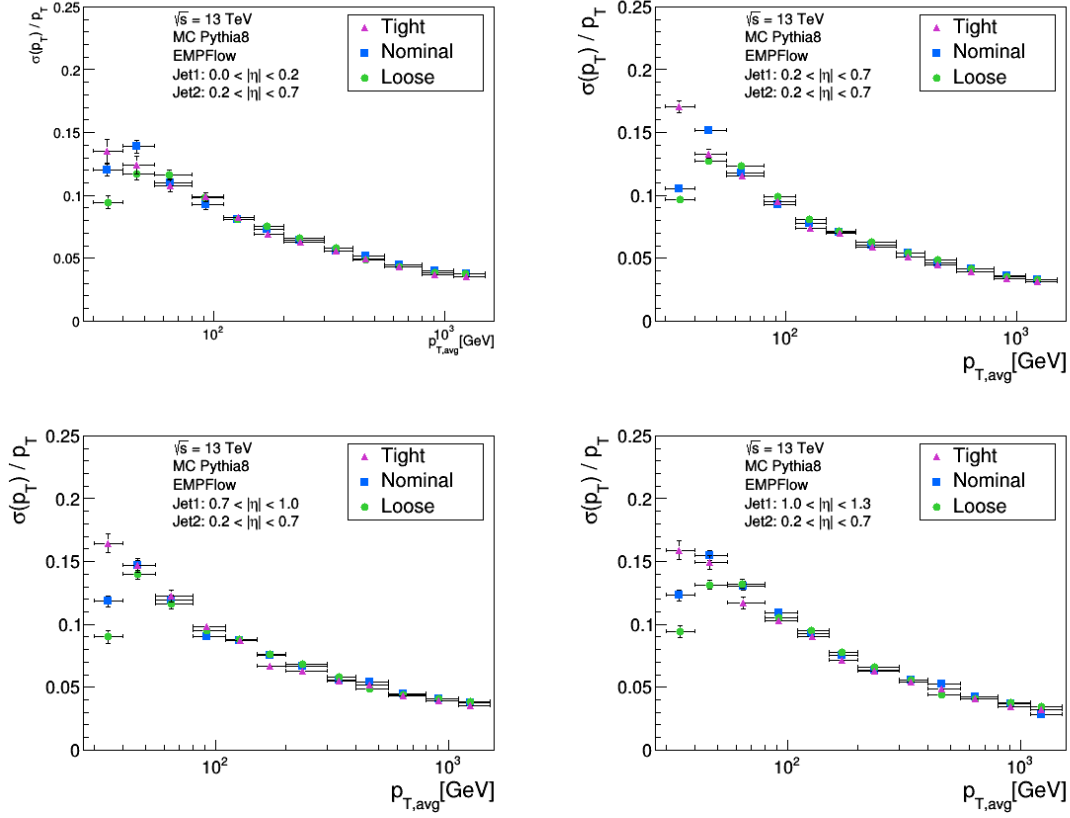
Figure D.3: Additional JER plots for MC Pythia8 tight, nominal and loose dijet selection are shown.
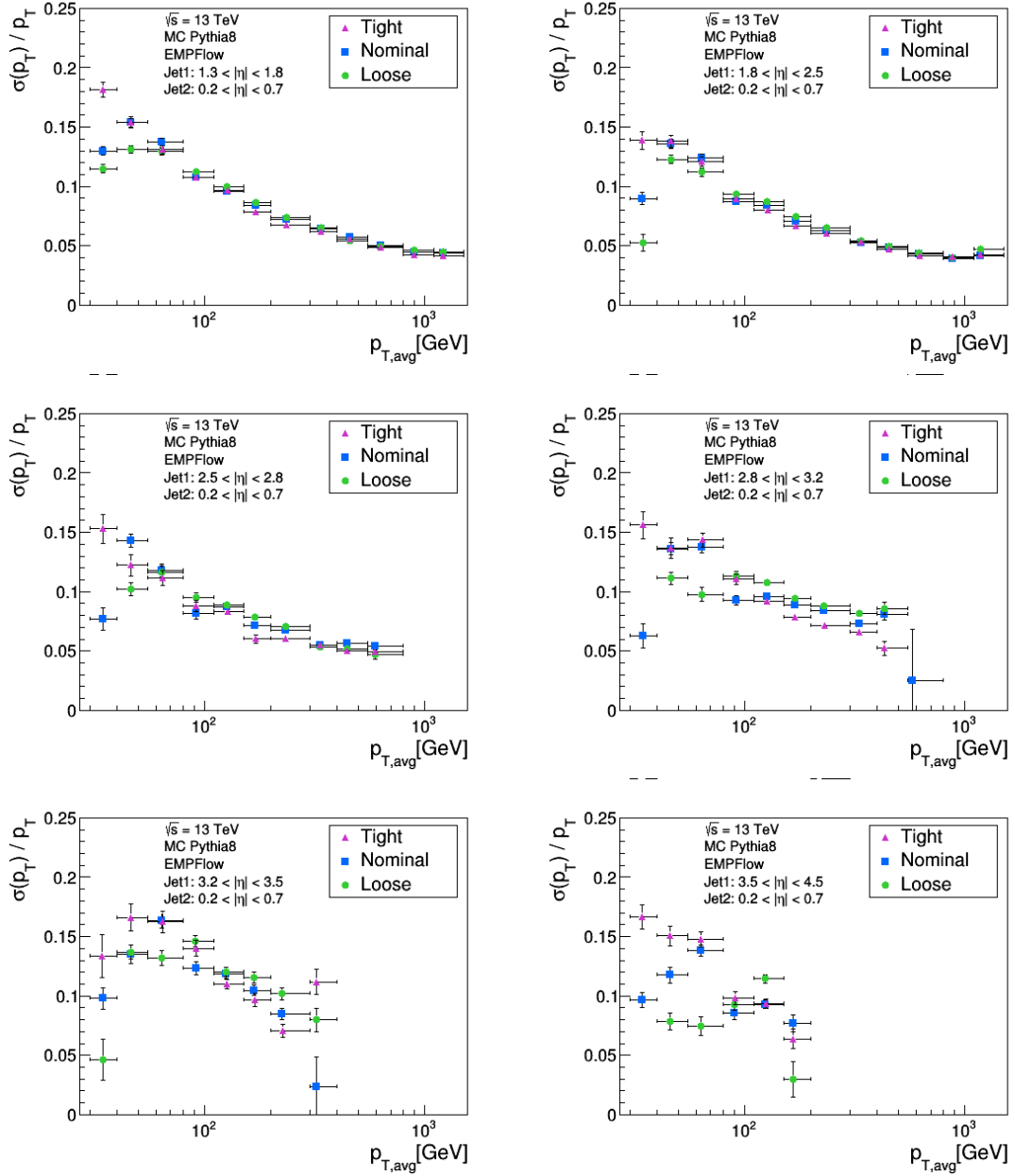
Figure D.4: Additional JER plots for MC Pythia8 tight, nominal and loose dijet selection are shown.

List of Figures

List of Tables

Acknowledgements